



Using grain boundary irregularity to quantify dynamic recrystallization in ice



Sheng Fan^{a,*}, David J. Prior^a, Andrew J. Cross^{b,c}, David L. Goldsby^b, Travis F. Hager^b, Marianne Negrini^a, Chao Qi^d

^a Department of Geology, University of Otago, Dunedin, New Zealand

^b Department of Earth and Environmental Science, University of Pennsylvania, Philadelphia, PA, United States

^c Department of Geology and Geophysics, Woods Hole Oceanographic Institution, Woods Hole, MA, United States

^d Institute of Geology and Geophysics, Chinese Academy of Sciences, Beijing, China

ARTICLE INFO

Article history:

Received 24 December 2020

Revised 7 March 2021

Accepted 10 March 2021

Available online 15 March 2021

Keywords:

High-temperature deformation

Grain boundary irregularity

Dynamic recrystallization

Grain boundary migration

Crystallographic orientation

Electron backscatter diffraction

ABSTRACT

Dynamic recrystallization is an important mechanical weakening mechanism during the deformation of ice, yet we currently lack robust quantitative tools for identifying recrystallized grains in the “migration” recrystallization regime that dominates ice deformation at temperatures close to the ice melting point. Here, we propose grain boundary irregularity as a quantitative means for discriminating between recrystallized (high sphericity, low irregularity) and remnant (low sphericity, high irregularity) grains. To this end, we analysed cryogenic electron backscatter diffraction (cryo-EBSD) data of deformed polycrystalline ice, to quantify dynamic recrystallization using grain boundary irregularity statistics. Grain boundary irregularity has an inverse relationship with a sphericity parameter, Ψ , defined as the ratio of grain area and grain perimeter, divided by grain radius in 2-D so that the measurement is grain size independent. Sphericity (Ψ) typically decreases with increasing grain size, up to a threshold grain size, above which Ψ either plateaus (at temperature, $T < -10$ °C) or increases much more gradually (at $T \geq -10$ °C). There is no apparent relationship between grain boundary sphericity and grain *c*-axis orientation even at very high temperatures (-4 and -5 °C), where GBM dominates, suggesting little crystallographic control on the activity of grain boundary migration (GBM). Decreasing sphericity up to the threshold grain size can be explained by newly-formed, small, spherical recrystallized grains growing via strain-induced GBM and thereby developing increasingly irregular grain boundaries. We suggest that the plateau (or gradual decrease) in sphericity at larger sizes represents a population of original grains (i.e., remnant grains) that becomes increasingly irregular (at similar rates) due to the balance between GBM and nucleation. In this interpretation, the threshold grain size represents the largest grain size reached by a growing recrystallized grain by the end of an experiment. Thus, grain boundary irregularity provides a means for discriminating between recrystallized and remnant grains—a capability that is potentially useful for evaluating dynamic recrystallization processes in ice deformed at temperatures close to the melting point. The threshold grain size and experiment duration can be used to calculate the rates of recrystallization and grain size evolution associated with GBM. Grain size evolution rates are similar at high and low temperatures, suggesting similar GBM rates. Previous studies show that grain boundary mobility decreases with decreasing temperature. The driving force of GBM, on the other hand, has a positive correlation with stress, which increases with a decreasing temperature if strain rate remains unchanged. The balance between boundary mobility and driving force is likely the cause of similar GBM rates between high and low temperatures.

© 2021 Acta Materialia Inc. Published by Elsevier Ltd. All rights reserved.

1. Introduction

Dynamic recrystallization is a process by which a crystalline aggregate lowers its free energy during plastic deformation, and has been studied as a mechanical weakening mechanism in many crystalline materials, including metals, ceramics, minerals, and water ice [1–4]. Dynamic recrystallization involves the migration and/or

* Corresponding author at: Department of Geology, University of Otago, 360 Leith Street, Dunedin, New Zealand

E-mail addresses: sheng.fan@otago.ac.nz, sheng.fan.geology@gmail.com (S. Fan), david.prior@otago.ac.nz (D.J. Prior), across@whoi.edu (A.J. Cross), dgoldsbys@sas.upenn.edu (D.L. Goldsby), marianne.negrini@otago.ac.nz (M. Negrini), qichao@mail.iggcas.ac.cn (C. Qi).

formation of grain boundaries during creep [3,5]. Strain energy heterogeneities drive grain boundaries to migrate from regions with low dislocation densities to regions with high dislocation densities. This process is known as strain-induced grain boundary migration (GBM), which is thought to favour the growth of grains with lower stored strain energies (i.e., grains with high Schmid factors) at the cost of grains with higher stored strain energies (i.e., grains with low Schmid factors) and, furthermore, often becomes more widespread at higher temperatures [6–9]. Localised strain-induced GBM, at where crystal lattice bends sharply or neighbouring grain boundaries are pinned, is likely to favour the production of “new” grains via bulge nucleation [3,10,11]. In addition, high-angle grain boundaries can form via a continuous input of dislocations into low-angle boundaries, which are produced from the dynamic recovery of dislocations [4,12,13]. Together, dynamic recovery and recrystallization can produce “new” recrystallized grains, which are usually strain-free, at the cost of “old” remnant grains that contain relatively high dislocation densities [3,5,14], thereby reducing stored strain energy. Thus, through the migration and/or formation of grain boundaries—as with grain nucleation—stored strain energy is reduced, work hardening (via dislocation multiplication and interaction) is counteracted, and mechanical weakening may be achieved [15–17]. Weakening is manifested as a strain rate enhancement from secondary to tertiary creep in constant load/stress experiments [18–20], or a stress reduction from peak to flow stress in constant displacement rate experiments [9,21,22]. The observation of severe grain size reduction within the high-strain interiors of natural and experimental shear zones [23–25] implies that dynamic recrystallization plays a crucial role in localizing strain in Earth’s lithosphere. Likewise, dynamic recrystallization is considered essential for the accumulation of large plastic strains in glaciers and ice sheets [26–28]. Thus, we need ways of identifying recrystallized grains to assess dynamic recrystallization processes and rates in experimentally and naturally deformed ice.

Following recent methodological advances [29–31], cryogenic electron backscatter diffraction (cryo-EBSD) has become a routine tool for quantifying grain size, grain shape, crystallographic preferred orientation (CPO) and plastic intragranular deformation in ice [7–9]. However, attempts to understand high temperature microstructures and recrystallization are hampered by challenges in identifying newly-formed recrystallized grains [32,33]. Moreover, ice grains deformed at high temperatures can have highly irregular and branching shapes in 3-D, and these grains are likely to be sampled multiple times in 2-D sections [34–36]. To isolate recrystallized grains in ice and other minerals, previous studies have typically applied an imposed cut-off value of grain size, or used measures of intragranular lattice distortion to identify small, low strain grains [37–39]. The cut-off grain size is usually defined as the central minimum in a bimodal grain size distribution [32,40], or is defined by an average subgrain size [37,41,42] based on the hypothesis that, during subgrain rotation recrystallization, recrystallized grains will have a similar size to the subgrains from which they form [3]. The most common measures of intragranular lattice distortions include dislocation density [38,43] and grain orientation spread (GOS) [39,44,45]. The segregation of recrystallized and remnant grains using dislocation density and GOS is based on the hypothesis that recrystallized grains should be initially strain-free [3,14,46], and should therefore have low dislocation densities and GOS values. These approaches usually work well with samples that were deformed at relatively low homologous temperatures, but often fail under high homologous temperature conditions that favour rapid GBM. GBM-dominated grains often have highly irregular boundaries and can give varying apparent grain sizes due to sectioning effects [33,35,36], while lattice distortion (a proxy for the density of geometrically necessary dislocations) often falls below the angular resolution of conventional EBSD in the

GBM-dominated regime [39]. Based on observations of concomitant dynamic recrystallization and *c*-axis cone development in uniaxial compression experiments on ice polycrystals [8,47], Cross and Skemer [48] defined recrystallized ice grains as those with high basal Schmid factors (i.e., with *c*-axes lying within a cone around the compression axis) when analysing the compressed ice samples of Vaughan and others [47]. However, this approach requires constraints on the orientation distributions within completely recrystallized and completely unrecrystallized samples (as upper and lower bounds, respectively), and, moreover, is unsuitable for samples with complex CPOs, such as those formed under complex loading geometries or histories.

Microstructural studies of deformed rock and ice samples suggest that grain boundary irregularity might evolve systematically during deformation [49–52]. Linked to this is the idea that remnant (original) grain boundaries might become increasingly irregular with increasing strain, due to the progression of dynamic recrystallization [3,27,53]. To evaluate grain boundary irregularity as a means for quantifying dynamic recrystallization at high temperatures, here we examine cryo-EBSD data collected from experimentally deformed ice samples. These samples were deformed to different finite strains, through the transition from secondary minimum to tertiary creep in constant load experiments at -4°C , or through the transition from peak to flow stresses in constant displacement rate experiments at -10 , -20 and -30°C . Most of the samples were deformed under uniaxial compression; however, we also deformed samples at -30°C under direct shear to achieve strains higher than those attainable in uniaxial compression. Samples included two different starting materials, with initial median grain sizes of ~ 300 and $550\ \mu\text{m}$. We processed the cryo-EBSD data to quantify grain boundary irregularity using methods similar to Takahashi and others [50], Hamann and others [52] and Heilbronner and Barrett [51]. Grain boundary irregularity and grain size statistics were used to distinguish recrystallized grains from remnant grains within deformed ice samples. The EBSD data, which provide full crystallographic orientations, were also used to identify grains that are likely oversampled in 2-D sections (i.e., limbs of the same branching grain that intersect the 2-D section multiple times). From this, we investigated how the stereological issue of oversampling affects the identification of recrystallized grains based on grain boundary irregularity and grain size. Overall, we propose that grain boundary irregularity can be used to reliably identify recrystallized grains in ice and, furthermore, gives insight into the physical processes driving microstructural evolution in ice at high temperatures.

2. Methods

2.1. Laboratory experiments

2.1.1. Sample fabrication

We prepared dense, cylindrical polycrystalline pure water ice samples with two different initial mean grain sizes of $\sim 300\ \mu\text{m}$ (fine-grained ice) and $\sim 550\ \mu\text{m}$ (medium-grained ice). These ice samples were fabricated using a flood-freeze method [22,54,55]. First, we prepared ice seeds (i.e., ice powders) with particle sizes limited between 180 and $250\ \mu\text{m}$ by sieving crushed ice cubes made from ultra-pure deionized water. Ice seeds were packed into lightly greased cylindrical moulds to achieve a porosity of $\sim 40\%$. Degassed ultra-pure deionized water (0°C) was then flooded into the packed moulds, which had been evacuated to a near-vacuum state and equilibrated at 0°C in a water-ice bath for ~ 40 min. The flooded moulds were immediately transferred to a -30°C chest freezer and placed vertically into cylindrical holes in a polystyrene block for ~ 24 h, with the base of moulds touching a copper plate at the bottom of the freezer. This procedure ensures the

freezing front migrates upwards, reducing the chance of trapping bubbles within the samples. Fine-grained ice samples were gently pushed out from the moulds using an arbor press. Medium-grained ice samples were accidentally made by equilibrating the frozen, flooded assembly of fine-grained ice and mould, with temperature of $-30\text{ }^{\circ}\text{C}$, at $0\text{ }^{\circ}\text{C}$ in a water-ice bath for ~ 30 min before extraction.

2.1.2. Deformation assembly

For uniaxial compression experiments, we prepared cylindrical ice samples with length-to-diameter ratios of between 1.5:1 and 2:1. Ice samples were cut and polished to ensure that their ends were flat and perpendicular to the cylinder axis. Uniaxial compression experiments are usually performed under constant load/stress [7,21,56] or under constant displacement rate conditions [8,9,22]. In this study, medium-grained ice ($\sim 550\text{ }\mu\text{m}$) samples were used for constant uniaxial load experiments, performed at the University of Otago, while fine-grained ice ($\sim 300\text{ }\mu\text{m}$) samples were used for constant uniaxial displacement rate experiments, performed at the University of Pennsylvania. For the constant load experiments, each medium-grained sample was encapsulated in a rubber jacket together with a walnut wooden platen and a walnut wooden piston attached tightly at each end. Encapsulation of the deformation assembly was completed in a $-30\text{ }^{\circ}\text{C}$ chest freezer. For the constant rate experiments, each fine-grained sample was encapsulated in a thin-walled indium jacket ($\sim 0.38\text{ mm}$ wall thickness) with the bottom already welded (melted) to a stainless-steel end-cap. The top of indium jacket tube was then welded to a steel semi-internal force gauge, with a thermally insulating zirconia spacer placed between the force gauge and sample. The deformation assembly was kept at $-60\text{ }^{\circ}\text{C}$ during welding by submergence in a cold ethanol bath.

Fine-grained ice samples also were used for direct shear experiments performed at the University of Pennsylvania. We prepared sliced ice samples following the procedures described by Qi and others [57]. Sliced ice samples were obtained by cutting cylindrical ice samples at 45° from the cylinder axis. Both cut surfaces were carefully polished to make sure they were flat and parallel to each other. The deformation assembly was comprised of a sliced ice sample fitted tightly between two 45° -cut aluminium pistons. 120-grit sandpaper was epoxied to the 45° cut surface of each piston to prevent slippage during deformation. Each deformation assembly was double jacketed using two indium tubes ($\sim 0.76\text{ mm}$ total wall thickness), with the outer indium tube already welded to a stainless-steel end-cap. The outer layer of the indium double jacket was then welded to a steel semi-internal force gauge, with a zirconia spacer placed between the force gauge and the top of deformation assembly. The deformation assembly was kept at $-60\text{ }^{\circ}\text{C}$ during welding by submergence in a cold ethanol bath.

2.1.3. Deformation experiments

Constant load, uniaxial compression experiments were conducted at $-4 \pm 0.2\text{ }^{\circ}\text{C}$ in a customized unconfined deformation rig in the Ice Physics Laboratory, University of Otago (Sect. S1 of the supplement). These experiments were conducted with a load of 60 kg, yielding an initial axial stress of $\sim 1.0\text{ MPa}$. Experiments were terminated once the true axial strain, ε , reached $\sim 1\%$, 4% , 8% and 13% .

Constant displacement rate, uniaxial compression and direct shear experiments were conducted in a cryogenic apparatus [22,58] under a nitrogen gas confining pressure of 20–40 MPa in the Ice Physics Laboratory, University of Pennsylvania. Most of these experiments were conducted at -10 , -20 and $-30\text{ }^{\circ}\text{C}$ under constant displacement rates yielding initial true axial strain rates, $\dot{\varepsilon}$, of $\sim 1 \times 10^{-5}\text{ s}^{-1}$; these experiments were terminated once the true axial strain, ε , reached $\sim 3\%$, 5% , 8% , 12% and 20% . Some fine-grained ice samples were deformed at $-30\text{ }^{\circ}\text{C}$ with $\dot{\varepsilon}$ of $\sim 6 \times$

10^{-5} s^{-1} ; these experiments were terminated once ε reached $\sim 3\%$ and $\sim 20\%$. Direct shear experiments were conducted at $-30\text{ }^{\circ}\text{C}$ under constant displacement rates, yielding initial shear strain rates, $\dot{\gamma}$, of $\sim 1.66 \times 10^{-5}\text{ s}^{-1}$ and $1.09 \times 10^{-4}\text{ s}^{-1}$ equivalent to von Mises strain rates, $\dot{\gamma}_v$, of $\sim 1 \times 10^{-5}\text{ s}^{-1}$ and $\sim 5 \times 10^{-5}\text{ s}^{-1}$, respectively. The experiments were terminated once the estimated shear strain, γ_{est} , reached ~ 1 , which is equivalent to von Mises strain, γ_v , of ~ 0.6 .

For all experiments, ice samples were left to thermally equilibrate with the deformation apparatus for at least 60 min at the experiment conditions (temperature and confining pressure) before deformation started. After each experimental run, samples were extracted from the apparatus, photographed, and measured. To minimize thermal cracking, samples were progressively cooled to ~ -30 , -100 and $-196\text{ }^{\circ}\text{C}$ over about 15 min, and thereafter stored in a liquid nitrogen dewar. Typical time between the end of the experiments and the start of cooling was between 10 and 30 min. Minor static recovery of the ice microstructures may happen on this timescale [59], but significant changes in ice microstructure are unlikely.

2.2. Cryo-EBSD data

Cryo-EBSD data were acquired at the University of Otago, using a Zeiss Sigma VP FEG-SEM, combined with a NordlysF or Symmetry EBSD camera from Oxford Instruments. Ice sample preparation and cryo-EBSD data acquisition were performed following the procedures described by Prior and others [60]. Data were collected at a stage temperature of $\sim -95\text{ }^{\circ}\text{C}$, with 2–7 Pa nitrogen gas pressure, 30 kV accelerating voltage and $\sim 60\text{ nA}$ beam current. Raw EBSD data were montaged using Oxford Instruments' Aztec software, enabling mapping of regions up to 40 mm by 70 mm in area. For fine-grained ice samples, we collected EBSD maps with the step size of $5\text{ }\mu\text{m}$; for medium-grained ice samples, we collected EBSD maps with a step size of $30\text{ }\mu\text{m}$. We have also re-analysed cryo-EBSD data acquired at a step size of $40\text{ }\mu\text{m}$ by Vaughan and others [47]. These data were collected from ice samples deformed at $-5\text{ }^{\circ}\text{C}$ under a constant displacement rate ($\sim 1.1 \times 10^{-6}\text{ s}^{-1}$) to finite true axial strains of $\sim 1\%$, 3% , 5% , 8% , 11% . Microstructural analyses were performed in the MTEX toolbox [61,62] in MATLAB.

2.2.1. Grain size

Ice grains were reconstructed from raw EBSD pixel maps using a Voronoi decomposition algorithm in the MTEX toolbox [61], with a grain boundary misorientation threshold of 10° . Grain size is defined here as the diameter of a circle with the area equal to the measured area of each grain. Grains with area equivalent diameter smaller than $20\text{ }\mu\text{m}$ (for EBSD maps with $5\text{ }\mu\text{m}$ step size) or $160\text{ }\mu\text{m}$ (for EBSD maps with $40\text{ }\mu\text{m}$ step size), which may result from mis-indexing, were removed. We also removed grains intersecting the edges of EBSD maps, as well as poorly constrained grains produced in regions of sparse pixel coverage—i.e., grains with $<50\%$ indexed pixel coverage were removed. Note that, due to stereological effects, grain sizes measured from a 2-D section will always underestimate the true 3-D grain size. We also calculated area frequency as a function of grain size.

2.2.2. Grain boundary irregularity

Deformed ice samples often contain large grains interlocking with smaller grains, with many irregular grain boundaries [7,9,53]. Boundary irregularity is hard to judge by visual inspection and it is better to use quantitative measures of boundary irregularity to infer processes across different deformation conditions [49,50]. Here, we quantified the irregularity of each grain's boundary by introducing a sphericity parameter Ψ , which is calculated from grain

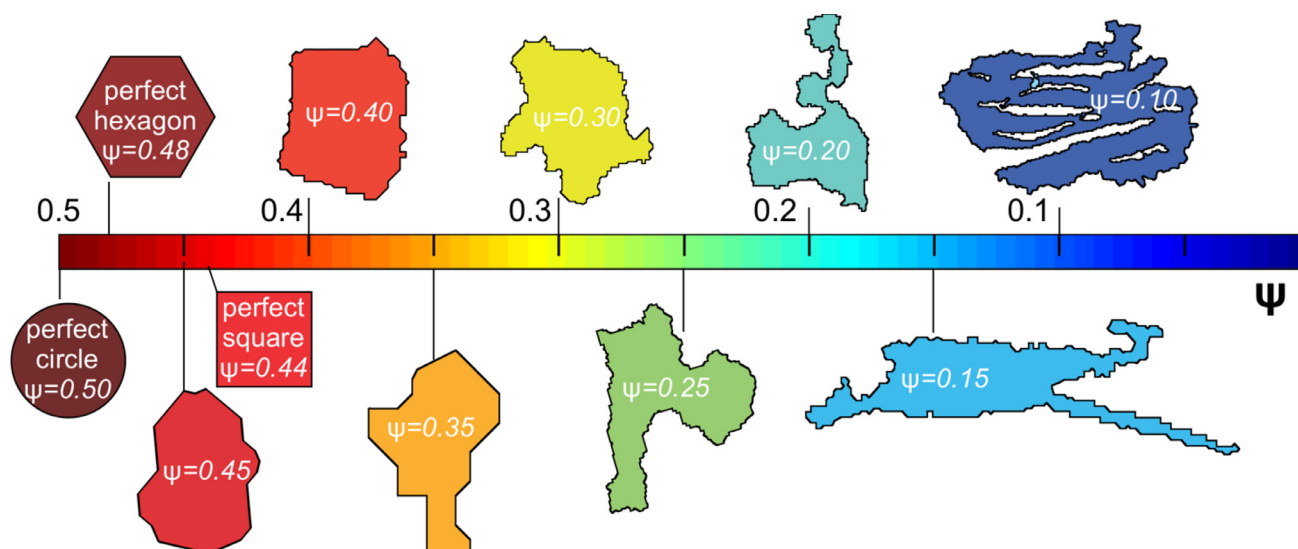


Fig. 1. Illustration of grains and geometric shapes with different sphericity parameter Ψ values. Sphericity is the measurement of grain boundary irregularity.

area, A , grain boundary perimeter, P , and area equivalent grain radius, R , in 2-D:

$$\Psi = \frac{A}{P \times R}. \quad (1)$$

Grain boundary sphericity, Ψ , is a useful indicator for grain boundary irregularity because Ψ measures how closely a grain's boundary resembles the circumference of a perfect circle. The Ψ decreases from 0.5, where the grain has a perfect circular shape, to 0, where the grain boundary is infinitely irregular. Examples of grains and specific geometric shapes with different Ψ values are illustrated in Fig. 1. This method is similar to that applied by Heilbronner and Bartett [51], Hamann and others [52] and Takahashi and others [50].

Grain boundary sphericity (i.e., irregularity) measurements depend on our ability to accurately resolve grain boundary features (e.g., serrations, undulations, bulges). The EBSD grain boundary maps are sensitive to both step size, which governs how pixelated grain boundaries appear, and grain boundary smoothing, which minimizes grain boundary pixelation at the risk of introducing artefacts and/or removing grain boundary features. We test the influence of EBSD step size and grain boundary smoothing on grain boundary sphericity measurements in Appendix A and Appendix B, respectively. These tests show that, for EBSD maps collected at step sizes of 5 and 30 μm (as in this study), sphericity measurements of unsmoothed grain boundaries are generally robust enough to be used for analysing grain boundary irregularity in ice.

2.2.3. Oversampling of highly irregular grains

Grains deformed at high temperatures can have highly irregular and branching shapes in 3-D [34–36] (Fig. 2(a)). In 2-D sections, these grains are likely to be oversampled, since limbs of the same grain might appear multiple times (Fig. 2(a)). EBSD data provide full crystallographic orientations, which can help us assess the likelihood of nearby grains in the 2-D map belonging to the same grain in 3-D [9]. For a given EBSD map, we group all grains with similar orientations (i.e., with mean orientations within 10° of one another) within a radius of 1 mm (for fine-grained ice deformed at $T \leq -10^\circ\text{C}$) or 5 mm (for fine- and medium-grained ice deformed at $T > -10^\circ\text{C}$), to constrain grains that are likely repeat-counted in 2-D (i.e., non-unique grains) (Fig. 2(b)). These thresholds probably overestimate the number of 2-D grains that are connected in 3-D: the sizes of 1 and 5 mm are close to or more than

double that of the largest grain in fine-grained ice and medium-grained ice, respectively. The misorientation angle of 10° is more than twice the median—and greater than the 75th percentile—in mis2mean angle (the misorientation angle between all pixels in a grain and the mean orientation of that grain) for all samples (Sect. S2 of the Supplement). Unique grains are calculated by simply removing non-unique grains from the grain population (Fig. 2(b)). These data allow us to estimate the number of “distinct” grains—all 2-D grains with similar orientations (non-unique grains) attributed to the same 3-D grain are counted as one grain—and, from this, the number density of “distinct” grains; i.e., the number of unique grains per unit area [9]. Grain statistics are provided in Table 1 and Sect. S3 of the supplement. To understand whether 3-D branching grains, appearing as non-unique grains in 2-D, will affect the quantification of recrystallized grains, we will compare the statistics of grain boundary sphericity between all grains (that consider the effect of branching grains) and unique grain (that completely remove the effect of branching grains) in Sect. 3.2.

2.3. Modified avrami law: estimate the area frequencies of recrystallized grains

In this study, we seek to identify recrystallized grains based on grain boundary sphericity. During deformation, the area or volume fraction of recrystallized grains should increase monotonically with increasing time and/or strain. More specifically, recrystallized fraction should follow a sigmoidal path with increasing time/strain, as described by the Johnson-Mehl-Avrami-Kolmogorov theory for phase transformations [63–65], where a given transformation accelerates to a peak rate, before decelerating to completion. Thus, we can test whether our recrystallized fraction estimates provide reasonable, Avrami-type recrystallization kinetics.

The Avrami theory is routinely used to describe the kinetics and progression of static, time-dependant recrystallization [66,67], but can also be modified to describe dynamic recrystallization as a function of strain [68,69]. Steinemann [70] was the first to use Avrami theory to evaluate the kinetics of dynamic recrystallization in ice, but only across a relatively narrow range of conditions (-1.9 to -11.5°C). Cross and Skemer [48] made a further modification to express the Avrami equations in terms of homologous temperature, based on dynamic recrystallization rates across a range of geological and engineering materials including ice. The modified Avrami

Oversampling of highly irregular grains in 2-D sections

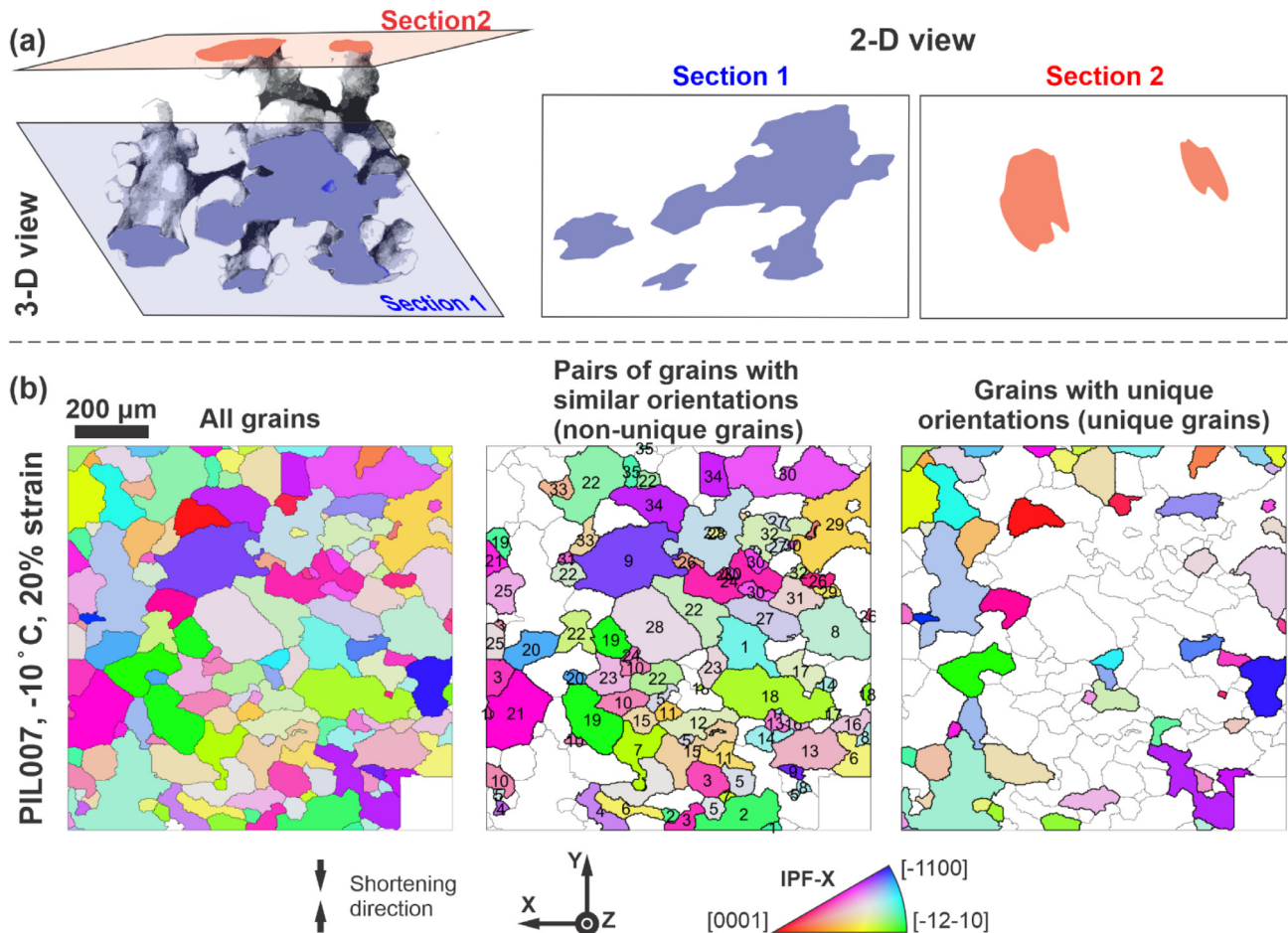


Fig. 2. (a) Illustrative drawing showing a typical 3-D ice crystal (adapted from Hooke and Hudleston [35]) deformed at high temperature, with its microstructure sampled by two thin sections. The planes of thin sections in 3-D are coloured by light blue or light red. Limbs of the ice grain sampled by thin sections are coloured by dark blue or dark red. (b) Illustration of the methods applied in this study to segregate grains that are likely to have non-unique and unique orientations (Sect. 2.2.3), with the data of fine-grained sample deformed to ~20% strain at -10 °C (PIL007) as an example. **Left box** shows all the grains within the selected area of orientation maps. Each grain is coloured by the mean orientation, coloured-coded by IPF-X, which uses the colour map to indicate the crystallographic axes that are perpendicular to the vertical shortening direction as shown by the black arrows. The colour-code of IPF-X is used to better identify differences in the misorientation angles between nearby grains. **Middle box** highlights grains that are likely to be repeat-counted in 2-D (non-unique grains). Grains that are misoriented by less than a 10° and within a 1 mm radius are considered as non-unique grains, and they are marked with the same number. **Right box** highlights grains with unique orientation (unique grains). These grains are calculated by simply removing non-unique grains from all grains. (For interpretation of the references to colour in this figure legend, the reader is referred to the web version of this article.)

law [48] is expressed as:

$$X = 1 - \exp\left(-C \exp\left(g \frac{T}{T_m}\right) (\Delta\varepsilon)^n\right), \quad (2)$$

where X is the area fraction of recrystallized grains, C is a pre-exponential constant, g is a rate constant that prescribes exponentially increasing dynamic recrystallization rates with linearly increasing homologous temperature, $\frac{T}{T_m}$, where T (K) is the deformation temperature and T_m (K) is the melting temperature of deformed material. $\Delta\varepsilon$ is the strain, ε , accommodated since the onset of dynamic recrystallization at the critical strain, ε_c : $\Delta\varepsilon = \varepsilon - \varepsilon_c$, and $\varepsilon_c = 0.71\varepsilon_p$, where ε_p is the strain at peak stress. Finally, n is the Avrami exponent—a constant that reflects the spatial and temporal dimensionality of grain nucleation and subsequent growth. Cross and Skemer [48] obtained best-fit parameters of $C = \exp(-10.0 \pm 3.86)$, $g = 13.8 \pm 5.15$, and $n = 1.6 \pm 0.34$ (95% confidence intervals). We will also directly compare our recrystallized frequency data predicted by grain boundary sphericity to those predicted by the modified Avrami law [48].

3. Results

3.1. Starting material

Undeformed fine- and medium-grained ice samples show a foam-like microstructure, characterized by straight grain boundaries and polygonal, equant grain shapes (Fig. 3(a)). Grain sizes of undeformed samples follow a unimodal, approximately log-normal distribution (Fig. 3(b)). Sphericity parameter (Ψ) values are mostly between 0.35 and 0.4 (Figs. 3(a), 3(c), 3(d)), indicating low grain boundary irregularity. All the undeformed samples have c -axis distributions that conform very closely to an expected random distribution of c -axes (Fig. 3(e))—in other words, grains are randomly orientated in the undeformed samples. Grains with different c -axes orientations have very similar Ψ values (Fig. 3(e)).

3.2. Deformed ice samples

3.2.1. Number density of distinct grains

Fig. 4 illustrates the change in the number density of distinct grains (counting 2-D grains with similar orientation as one in 3-D,

Table 1
Summary of statistics of mechanical, sphericity parameter and grain size data.

Deformation condition	No.	T (°C)	Stress (MPa)	^a Equivalent strain rate (/s)	^b Equivalent strain (%)	^c Strain since estimated onset of DRX (%)	Number of grains			Number density (number per unit area) of distinct grains (/μm ²)	Number density of distinct grains as ratio to the starting material	All grains: ^f grain size threshold interval for separating grains with “low” and “high” sphericity parameters (μm)	Unique grains: grain size threshold interval for separating grains with “low” and “high” sphericity parameters (μm)	All grains: ^g area fraction interval for grains with “high” sphericity parameters (%)	Unique grains: area fraction interval for grains with “high” sphericity parameters (%)	^h Estimated area frequency of DRX grains (%)
							All grains	^d Unique grains	^e Distinct grains							
Constant load, medium-grained ice	Undeformed			N/A			653	552	600	3.055E-6	1			N/A		
	OIL009	-4	1.02	1.11E-6	1	N/A	705	389	534	2.542E-6	0.832	N/A	177/200/223	N/A	2/4/6	0
	OIL008		0.99	1.40E-6	4	2.58	1716	600	1037	1.784E-6	0.584	187/426/666	12/292/571	8/8/24	0/3/18	12.5
	OIL007		0.95	1.78E-6	8	6.58	1569	382	779	1.420E-6	0.465	312/641/967	319/446/575	4/21/43	4/10/19	40.5
	OIL006		0.90	1.22E-6	13	11.58	2309	426	993	2.500E-6	0.717	533/767/1001	350/666/982	30/53/72	14/47/71	70.7
* Constant displacement rate, fine-grained ice	Undeformed			N/A			921	611	754	6.213E-6	1			N/A		
	def014	-5	1.13	1.00E-6	1	N/A	1881	1017	1404	6.395E-6	1.029	N/A	N/A	N/A	N/A	0
	def013		1.13	1.03E-6	3	2.38	8601	3051	5376	3.349E-6	0.539	365/574/783	370/576/781	13/43/79	13/41/77	6.4
	def012		1.22	1.05E-6	5	4.32	3143	1123	1928	2.896E-6	0.466	240/333/426	142/458/774	3/9/18	0/22/64	18.2
	def011		1.17	1.08E-6	8	7.43	5251	1412	2795	2.582E-6	0.416	241/353/465	208/413/618	4/12/22	2/17/38	38.9
def010		1.20	1.11E-6	11	10.29	4622	1221	2401	1.897E-6	0.305	385/525/665	324/570/815	12/21/33	7/24/46	52.1	
Constant displacement rate, fine-grained ice	Undeformed			N/A			1242	1152	1186	9.970E-6	1			N/A		
	PIL176	-10	1.70	1.04E-5	3	1.58	548	236	371	2.050E-5	2.056	76/103/130	65/75/84	2/4/6	1/1/1	5
	PIL163		2.42	1.06E-5	5	4.29	1282	454	770	3.211E-5	3.221	80/120/161	84/151/218	4/14/26	4/21/39	14.5
	PIL178		1.97	1.19E-5	8	6.58	894	244	488	2.519E-5	2.527			N/A		31.8
	PIL177		1.90	1.21E-5	12	9.87	1300	308	646	3.262E-5	3.272	87/182/277	184/202/221	9/40/72	39/47/56	49.2
PIL007		1.33	1.22E-5	19	17.58	1523	705	984	5.031E-5	5.046	53/143/232	151/191/231	3/32/67	37/50/63	82.4	

(continued on next page)

Table 1 (continued)

Deformation condition	No.	T (°C)	Stress (MPa)	^a Equivalent strain rate (1/s)	^b Equivalent strain (%)	^c Strain since estimated onset of DRX (%)	Number of grains			Number density (number per unit area) of distinct grains (μm^b)	Number density of distinct grains as ratio to the starting material	All grains: ^f grain size threshold interval for separating grains with "low" and "high" sphericity parameters (μm)	Unique grains: grain size threshold interval for separating grains with "low" and "high" sphericity parameters (μm)	All grains: ^g area fraction interval for grains with "high" sphericity parameters (%)	Unique grains: area fraction interval for grains with "high" sphericity parameters (%)	^h Estimated area frequency of DRX grains (%)
							All grains	^d Unique grains	^e Distinct grains							
	PIL254	-20	4.25	1.06E-5	3	1.58	699	311	468	3.569E-5	3.580	82/91/100	117/138/160	6/6/6	8/10/12	3.1
	PIL182		4.44	8.94E-6	4	2.58	744	391	547	2.739E-5	2.747	57/78/99	74/86/98	1/3/5	2/2/3	5.8
	PIL184		3.24	1.17E-5	8	5.16	1001	330	586	3.163E-5	3.173	129/159/189	118/135/153	14/21/28	11/16/21	12.6
	PIL185		3.68	1.19E-5	12	9.87	2579	705	1389	6.953E-5	6.974	106/134/162	130/153/175	27/36/42	39/46/49	33.5
	PIL255		2.93	1.28E-5	20	17.87	2701	386	1058	8.323E-5	8.348	89/150/211	199/208/217	36/69/84	85/87/89	64.9
	PIL165	-30	8.15	1.09E-5	3	0.87	4923	3076	3911	3.020E-5	3.029	75/99/123	59/94/128	3/5/8	1/4/7	6.2
	PIL162		7.87	1.10E-5	5	2.87	2098	1009	1467	5.235E-5	5.251	105/138/172	90/120/151	15/25/35	10/20/28	3.5
	PIL164		7.31	1.07E-5	7	4.87	1259	611	881	4.718E-5	4.732	101/135/170	99/134/170	13/18/24	13/20/27	7.8
	PIL166		6.45	1.20E-5	12	9.87	5447	1407	2928	9.964E-5	9.994	138/233/328	206/282/358	56/75/92	75/88/98	21.8
	PIL268		5.00	1.31E-5	21	19.58	6809	1946	3751	7.546E-5	7.569	77/87/96	81/92/102	16/18/19	19/21/22	52.6
	*PIL267, S		3.20	9.58E-6	61	56.03	20,229	1935	6179	9.153E-5	9.181	137/164/190	152/181/209	75/81/86	86/88/89	97.9
	*PIL267, P						5205	642	1816	1.210E-4	12.096	118/144/170	148/172/196	64/74/76	90/92/94	
	PIL266	-30	11.26	5.40E-5	3	0.87	1342	855	1080	3.885E-5	3.897	70/89/108	92/102/113	3/5/7	6/7/8	6.2
	PIL243		7.35	6.70E-5	24	21.87	9259	1658	4285	1.363E-4	13.671	100/141/182	117/162/208	44/55/62	52/61/68	58.1
	*PIL260, S		7.89	6.27E-5	62	57.03	15,211	2794	6807	1.110E-4	11.133	106/115/125	103/123/144	37/39/40	46/50/52	98.2
	*PIL260, P						8783	1428	3670	1.258E-4	12.618	102/121/141	22/147/161	46/48/51	68/69/70	

^a Strain rate at the end of experiments. The strain rate is true axial strain rate for uniaxial compression experiment, and it is von Mises strain rate for direct shear experiment (marked with *).

^b Strain at the end of experiments. The strain is true axial strain for uniaxial compression experiment, and it is von Mises strain for direct shear experiment (marked with *).

^c Strain at the end of experiment subtracts estimated strain corresponding to the onset of dynamic recrystallization (DRX). The estimated strain corresponding to the onset of DRX is calculated from peak equivalent strain following the method described in Sect. 2.3.

^d Grains that are unlikely repeat-counted (unique grains) are calculated by removing non-unique grains from all the grains. Non-unique grains are nearby grains with a misorientation (calculated from mean orientations) less than 10° , within a radius of 1 mm (for fine-grained ice deformed at -10 , -20 and -30 °C) or 5 mm (for fine- and medium-grained ice deformed at -4 and -5 °C).

^e All 2-D grains with similar orientations (non-unique grains) attributed to the same 3-D grain are counted as one grain.

^f Method see Sect. 3.2.3. Lower limit, best fit and higher limit of the grain size threshold are separated by "/". The best fit grain size threshold is bold.

^g Method see Sect. 3.2.4. Area fractions corresponding to lower limit, best fit and higher limit of the grain size threshold are separated by "/". Area fraction corresponding to the best fit grain size threshold is bold.

^h Estimated from the modified Avrami law (Eq. (2), Cross and Skemer [40]).

* EBSD data from Vaughan and others [22].

* Direct shear experiments. "S" represents shear plane, "P" represents profile plane. The orientations of shear plane and profile plane relative to the deformed ice sample are illustrated in Fig. S5 of the supplement.

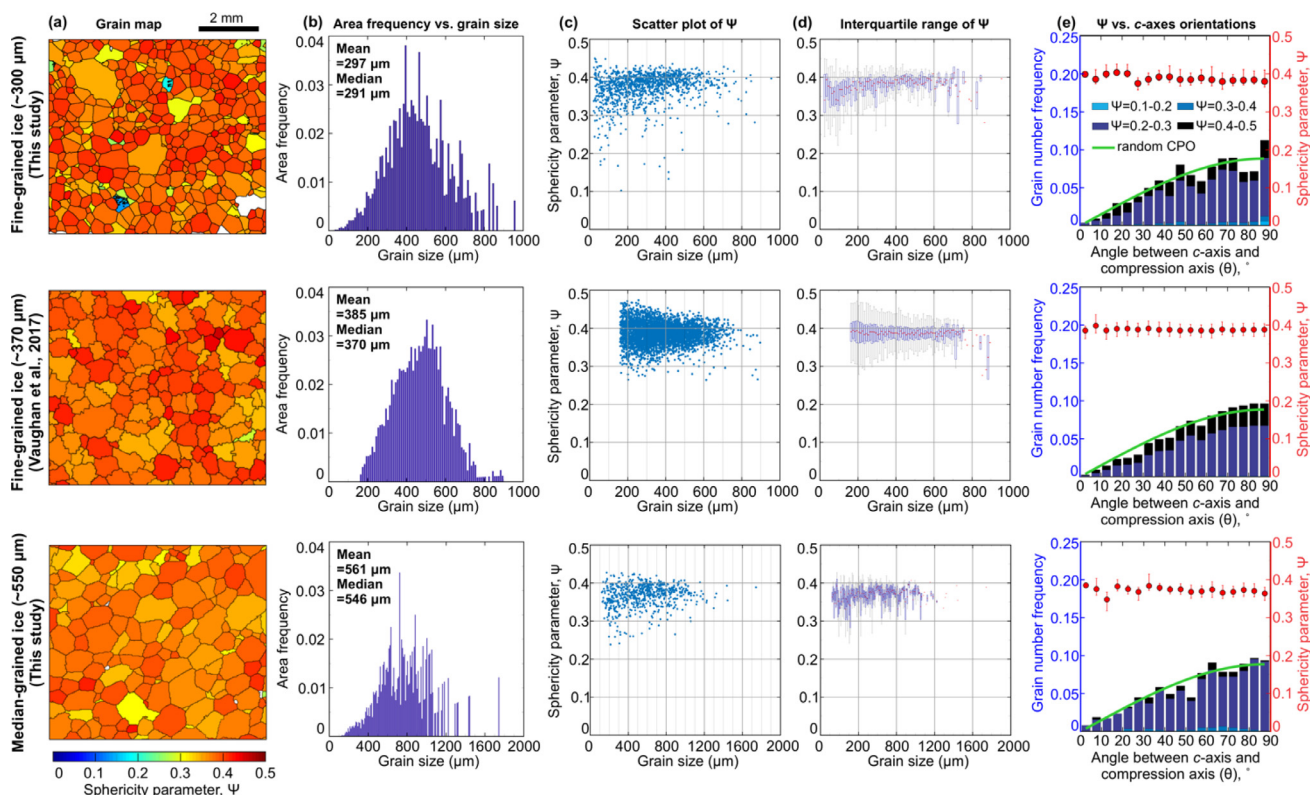


Fig. 3. Microstructural details of undeformed ice samples. We only show selected areas of EBSD maps so that the reader can resolve microstructural features. Quantitative microstructural analyses are based on much larger areas than those presented in the figures. (a) Grain maps with each grain coloured by corresponding grain boundary sphericity parameter, Ψ . Grain boundaries are black. (b) Area frequency as a function of grain size with a bin width of $10\mu\text{m}$. Mean and median grain sizes weighted by grain number frequencies are marked in top left corner. The relationship between Ψ and grain size is shown as scattered plot and interquartile range (IQR) with a bin width of $10\mu\text{m}$ in (c) and (d), respectively. IQR is visualised as box plot, the blue box covers the interquartile range and represents 50% of the total data, the red line within the box is the median point and the whiskers are the extremes. (e) Bar plots represent the number frequency (corresponds to the left y-axis) of grains with different Ψ as a function of c -axes angles to compression axis, θ (calculated from the mean orientation). Green line shows data expected from a random c -axes distribution. Error bar plots represent the IQR range (corresponds to the right y-axis) of grains with different Ψ as a function of θ . The red circle is the median point, the whiskers cover the interquartile range and represents 50% of the total data. Data from all grains in undeformed samples are used in the calculations. (For interpretation of the references to colour in this figure legend, the reader is referred to the web version of this article.)

Sect. 2.2.3) as a function of strain (Fig. 4(a)) and stress (Fig. 4(b)), for all samples deformed under uniaxial compression. Full details are outlined in Table S2 of the Supplement and key outcomes are listed in Table 1. Under relatively fast strain rates ($\dot{\epsilon} \geq \sim 1 \times 10^{-5}\text{s}^{-1}$) at temperatures of $T \leq -10^\circ\text{C}$, differential stresses are generally $\geq 2\text{MPa}$ (Table 1). Under these conditions, the number density of distinct grains generally increases with increasing strain (at a given temperature) or with decreasing temperature (at a given strain) (Fig. 4(a)). Under a relatively slow strain rate ($\dot{\epsilon} \approx \sim 1 \times 10^{-6}\text{s}^{-1}$) at $T > -10^\circ\text{C}$, differential stresses are close to 1MPa (Table 1). Under these conditions, the number density of distinct grains is less than that of the starting material, and it generally decreases with increasing strain (Fig. 4(a)). The number density of distinct grains (compared with the starting material) also generally increases with increasing differential stress (for a given strain) (Fig. 4(b)).

3.2.2. Grain area frequency

Sphericity and grain size analyses are illustrated in Figs. 5 and 6 for ice samples deformed at -4°C and -20°C , respectively. Full data sets are presented in Sect. S4 of the supplement. In each sample, the “all grains” and “unique grains” (grains with unique orientations, Sect. 2.2.3) populations have similar grain size distributions and patterns of sphericity parameter (as a function of grain size) (Figs. 5, 6, Sect. S4 of the supplement).

Fig. 7(a) illustrates patterns of grain area frequency as a function of grain size summarised from data of all ice samples, with

examples of deformed samples shown in Figs. 5(b), 6(b). For samples deformed at temperatures of $T \geq -10^\circ\text{C}$, grains follow a unimodal, normal distribution (Fig. 5(b), Fig. 7(a) red curves), centred around a peak value lower than that observed in the undeformed starting material (Fig. 3(b), Fig. 7(a) grey curve). The distribution also broadens to larger grain sizes with increasing strain (compare dashed and solid red curves, Fig. 7(a)). Samples deformed at temperatures of $T < -10^\circ\text{C}$, on the other hand, follow bimodal distributions, particularly at intermediate strains (Fig. 6(b), Fig. 7(a) blue curves), with one peak at fine grain sizes, and another at similar grain sizes to the undeformed starting material (e.g., PIL185, Fig. 6(b)). With increasing strain, the peak at smaller grain sizes grows at the expense of the peak at larger grain sizes (e.g., compare samples PIL254 and PIL255 in Fig. 6(b)).

3.2.3. Sphericity parameter and grain size

Sphericity, Ψ , generally decreases with increasing grain size, i.e., smaller grains are generally more spherical (e.g., Figs. 5(c), 6(c)). Sphericity also decreases with increasing strain (e.g., compare PIL254 and PIL255 in Fig. 6(c)); that is, grains generally become more irregular through the course of an experiment (Figs. 5(c), 6(c)). To quantify the relationship between Ψ and grain size, we extracted median Ψ values within grain size classes of $10\mu\text{m}$ bin width (e.g., Figs. 5(c), 6(c), Sect. S4 of the supplement). For all deformed samples, median Ψ values decrease with increasing grain size for smaller grains, up to a threshold grain size beyond which there is a change in slope of the sphericity

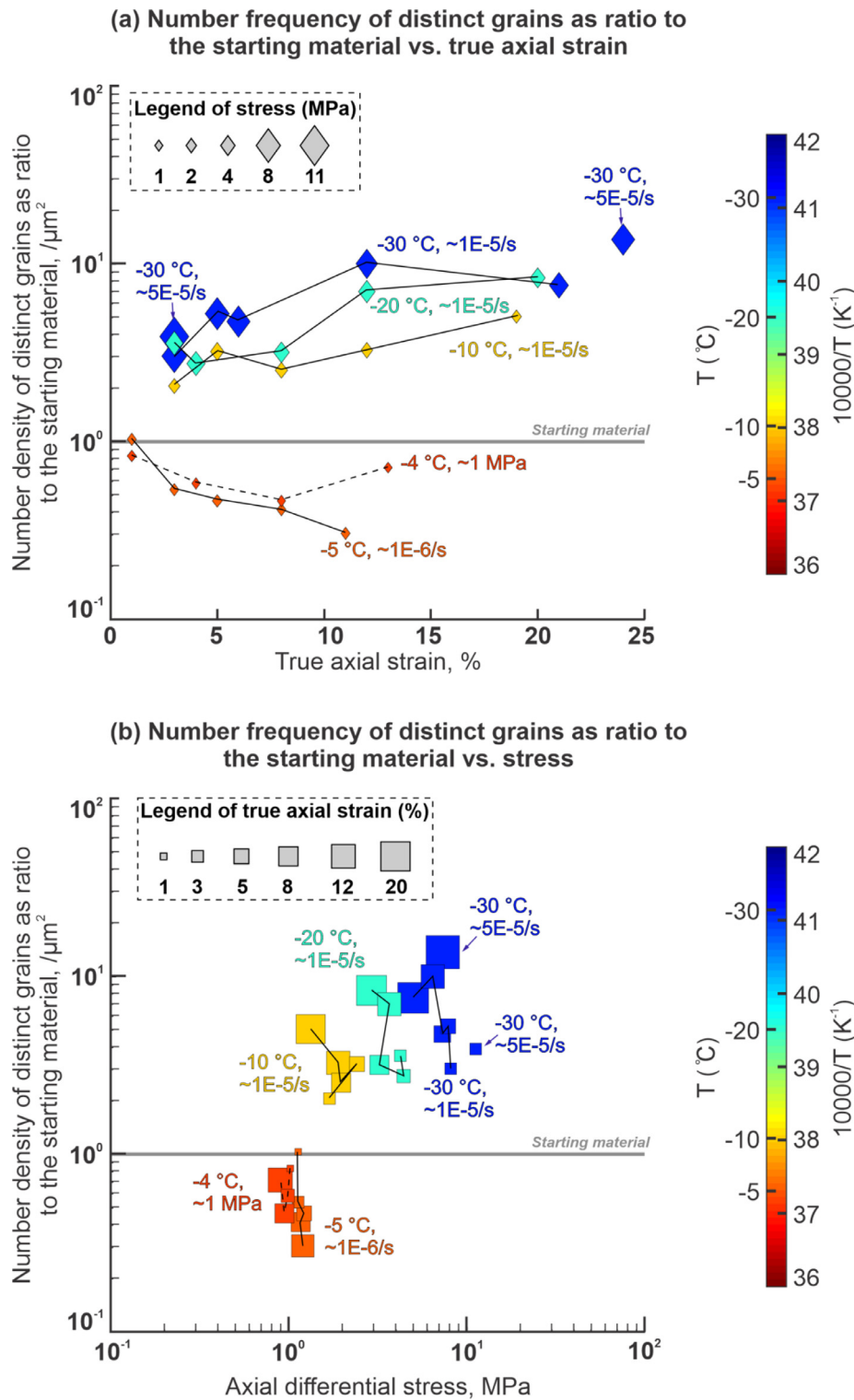


Fig. 4. Statistics of number density (grain number per unit area) of distinct grains (account 2-D grains with similar orientations as one grain in 3-D) for samples deformed under uniaxial compression. The number density of distinct grains is plotted as a function of (a) true axial strain, and (b) axial differential stress. At the same temperature, samples deformed at similar strain rate and stress are grouped by solid line and dashed line, respectively.

– grain size data (Figs. 5(c), 6(c), 7(b)). For samples deformed at $T \geq -10^\circ\text{C}$, the slope of median Ψ values (as a function of grain size) is shallower for larger grains than smaller grains (e.g., Figs. 5(c), 7(b)). For samples deformed at $T < -10^\circ\text{C}$, median Ψ values remain virtually constant over larger grain sizes (e.g., Fig. 6(c), 7(b)). Thus, two linear trends are observed in sphericity

– grain size space: a steeper trend at smaller grain sizes, and shallower trend at larger grain sizes (Figs. 5(d), 6(d), 7(b)). These linear trends intersect at a typical grain size of 300–800 μm for fine- and medium-grained ice deformed at $T > -10^\circ\text{C}$ (Fig. 5(d)), and 100–200 μm for fine-grained ice deformed at $T \leq -10^\circ\text{C}$ (Fig. 6(d)). The grain size at which the linear trends intersect tends to in-

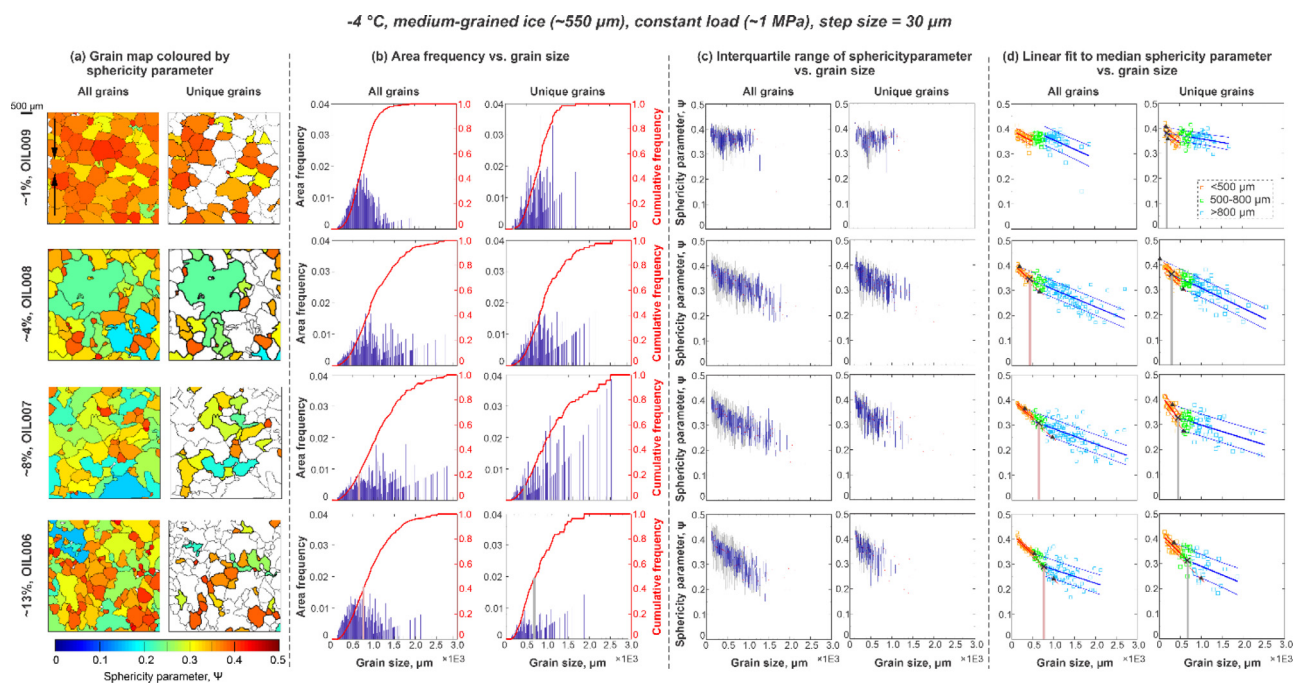


Fig. 5. Statistical analyses of grain size and grain shape for ice samples deformed at -4°C . For each panel (separated by grey dashed lines), they left column shows statistics of all grains, the right column shows statistics of unique grains (Sect. 2.2.3). **(a)** Microstructural map, with each grain coloured by sphericity parameter, Ψ . **(b)** Bar plots of grain area frequency as a function of grain size overlapped with line charts of cumulative grain area frequency as a function of grain size. The vertical thick pink and grey line represents the threshold grain size corresponding to (d). **(c)** Interquartile range (IQR) of Ψ as a function of grain size. The bin width of IQR is $10\ \mu\text{m}$. IQR is visualised as box plot, the box covers the interquartile range and represents 50% of the total data, the red line within the box is the median point and the whiskers are the extremes. **(d)** Scatter plots of median Ψ value for each grain size class with a bin width of $10\ \mu\text{m}$. Imposed grain size thresholds were applied to separate smaller and larger grains. The upper grain size limit for smaller grains is $100\ \mu\text{m}$ for fine-grained ice deformed at $T \leq -10^{\circ}\text{C}$, and it is $500\ \mu\text{m}$ for fine- and medium-grained ice deformed at $T > -10^{\circ}\text{C}$. The lower grain size limit for larger grains is $200\ \mu\text{m}$ for fine-grained ice deformed at $T \leq -10^{\circ}\text{C}$, and it is $800\ \mu\text{m}$ for fine- and medium-grained ice deformed at $T > -10^{\circ}\text{C}$. Linear fits were applied on the median Ψ -grain size data for smaller and larger grains, separately. Linear fits comprise the best linear fit (thick lines) and upper and lower bound of linear fit, i.e., best linear fit $\pm 95\%$ standard error (thin lines). Linear fit intersections of upper bounds of the linear fits and lower bound of the linear fits between smaller and larger grain data are marked as cross marks. Linear fit intersections of best fits between smaller and larger grain data are marked as cross marks. The vertical thick pink or grey line shows threshold grain size corresponding to the intersection of the best linear fit data. (For interpretation of the references to colour in this figure legend, the reader is referred to the web version of this article.)

crease with increasing strain (e.g., compare PIL254 and PIL255 in Fig. 6(d)).

3.2.4. Estimating the area frequencies of grains with high sphericity parameters

For each deformed sample, we calculated a “best fit” grain size threshold for separating grains with low and high sphericities, based on the intersections of linear fits through the sphericity-grain size data. We also calculate upper and lower threshold grain size bounds, based on the linear regressions plus/minus a 95% confidence interval (Table 1, Figs. 5(d), 6(d), Sect. S4 of the supplement). Lower bound, best-fit, and higher bound area frequencies of high- Ψ grains can thus be calculated from the lower bound, best-fit, and higher bound grain size thresholds, respectively (Table 1, Figs. 5(b), 6(b), Sect. S4 of the supplement). We calculated these parameters using the data of all grains and unique grains (Sect. 2.2.3), separately.

We plot the area frequency of grains with high Ψ as a function of strain accommodated since the estimated onset of dynamic recrystallization, $\Delta\varepsilon$ (Sect. 2.3), grouped by temperature (Fig. 8). The grain size threshold interval and area frequency of grains with high Ψ are generally comparable between all grains and distinct grains (Table 1, Fig. 8). For samples deformed in this study (-4 , -10 , -20 and -30°C series), the area frequency of grains with high Ψ generally increases with strain, but the trend is not simple (Figs. 8(a), 8(c-e)). At -30°C , the area frequencies of grains with high Ψ are similar for samples with equivalent strains (true axial strain for uniaxial compression, von Mises strain for direct shear) higher than $\sim 20\%$ (Fig. 8(e)). As a comparison, we also calculate

the area frequency range of recrystallized grains predicted by the modified Avrami law (grey lines in Fig. 8, Sect. 2.3). The area frequency ranges of recrystallized grains estimated from the modified Avrami law fall close to the area frequencies of high Ψ grains at $\Delta\varepsilon \leq \sim 20\%$ (Fig. 8(a), 8(c-e)).

For ice samples from Vaughan and others [47] the range of area frequencies of grains with high sphericity (illustrated by error bars) overlaps with area frequency ranges of recrystallized grains estimated by the modified Avrami law (illustrated by grey lines) (Fig. 8(b)). However, they show different patterns of evolution with strain: area frequencies of grains with high sphericity are similar at low and high strains, area frequencies of recrystallized grains estimated by the modified Avrami law increases with strain (Fig. 8(b)). One explanation for such a mismatch is that the EBSD data for these samples were collected at $40\ \mu\text{m}$ EBSD step size, which is too coarse for an accurate measurement of grain boundary sphericity (Appendix A), and it is thus prone to error in estimating the frequency of recrystallized grains.

3.2.5. Sphericity parameter and crystallographic orientations

To investigate the relationship between grain boundary irregularity and grain crystallographic orientations, we calculated the grain number frequency within Ψ ranges of 0.1 – 0.2, 0.2 – 0.3, 0.3 – 0.4 and 0.4–0.5, as well as interquartile range (IQR) of Ψ , for grains with c -axes at 5° intervals from the compression axis, using the data of all grains within each sample (e.g., Fig. 9, Sect. S5 of the supplement). For each grain, the angle between the c -axis and compression axis, θ , is calculated (from the mean orientation of each grain). For each Ψ range at each θ interval, the number

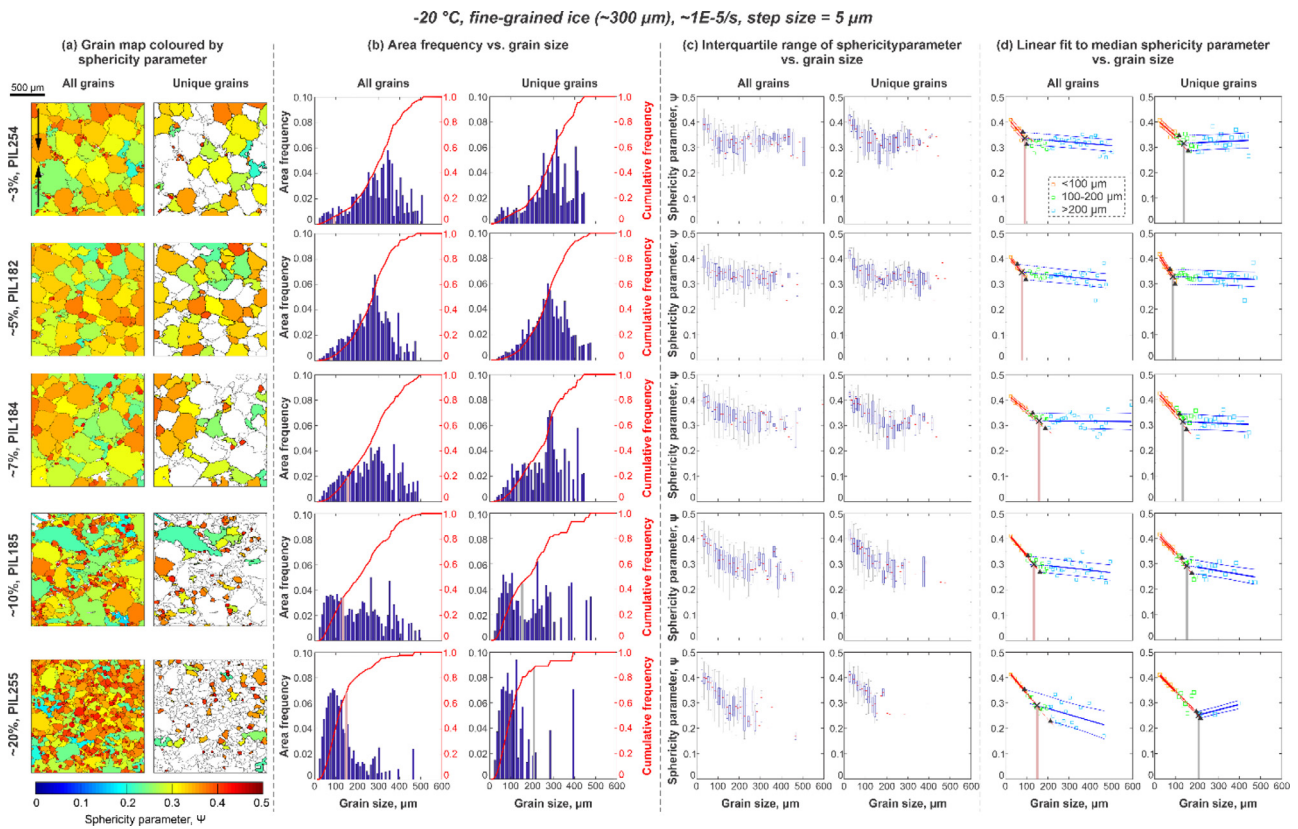


Fig. 6. Statistical analyses of grain size and grain shape for ice samples deformed at $-20\text{ }^{\circ}\text{C}$. Descriptions of (a) to (d) are the same as Fig. 5.

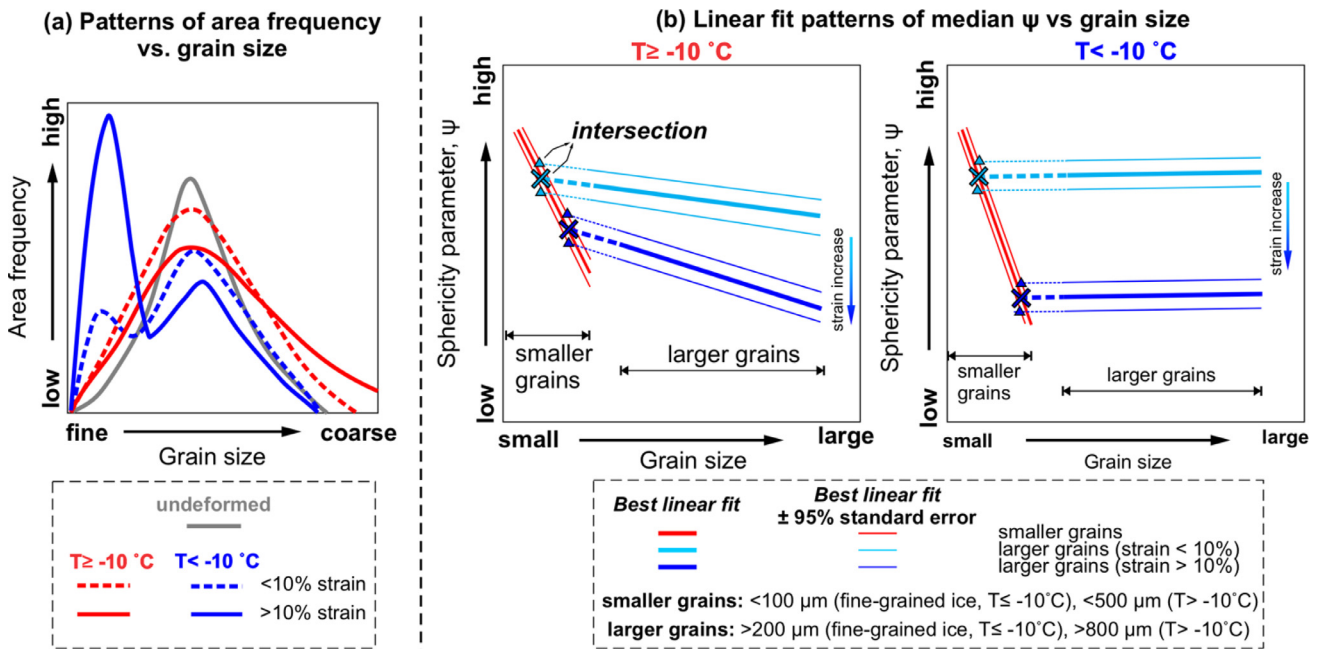


Fig. 7. (a) Patterns of area frequency as a function of grain size summarised from data of all ice samples, with examples shown in Figs. 5(b), 6(b). (b) Summarised linear fits of patterns of ψ data from data of all deformed samples, with examples shown in Figs. 5(d), 6(d). Cross marks represent intersections of the best linear fits for smaller and larger grains. Triangles represent intersections of upper bounds or lower bounds of the linear fits (best linear fit \pm 95% standard error) for smaller and larger grains. .

frequency of grains is calculated from the corresponding number of grains divided by the total number of grains for the smaller grain category or larger grain category within deformed samples. The smaller and larger grain category separately show that grains with different c -axes orientations have similar ranges of ψ values (Fig. 9, Sect. S5 of the supplement).

4. Discussion

4.1. Recrystallization processes

Lobate, interlocking grain boundaries are developed at strains higher than $\sim 3\%$ at all temperatures, and are commonly inter-

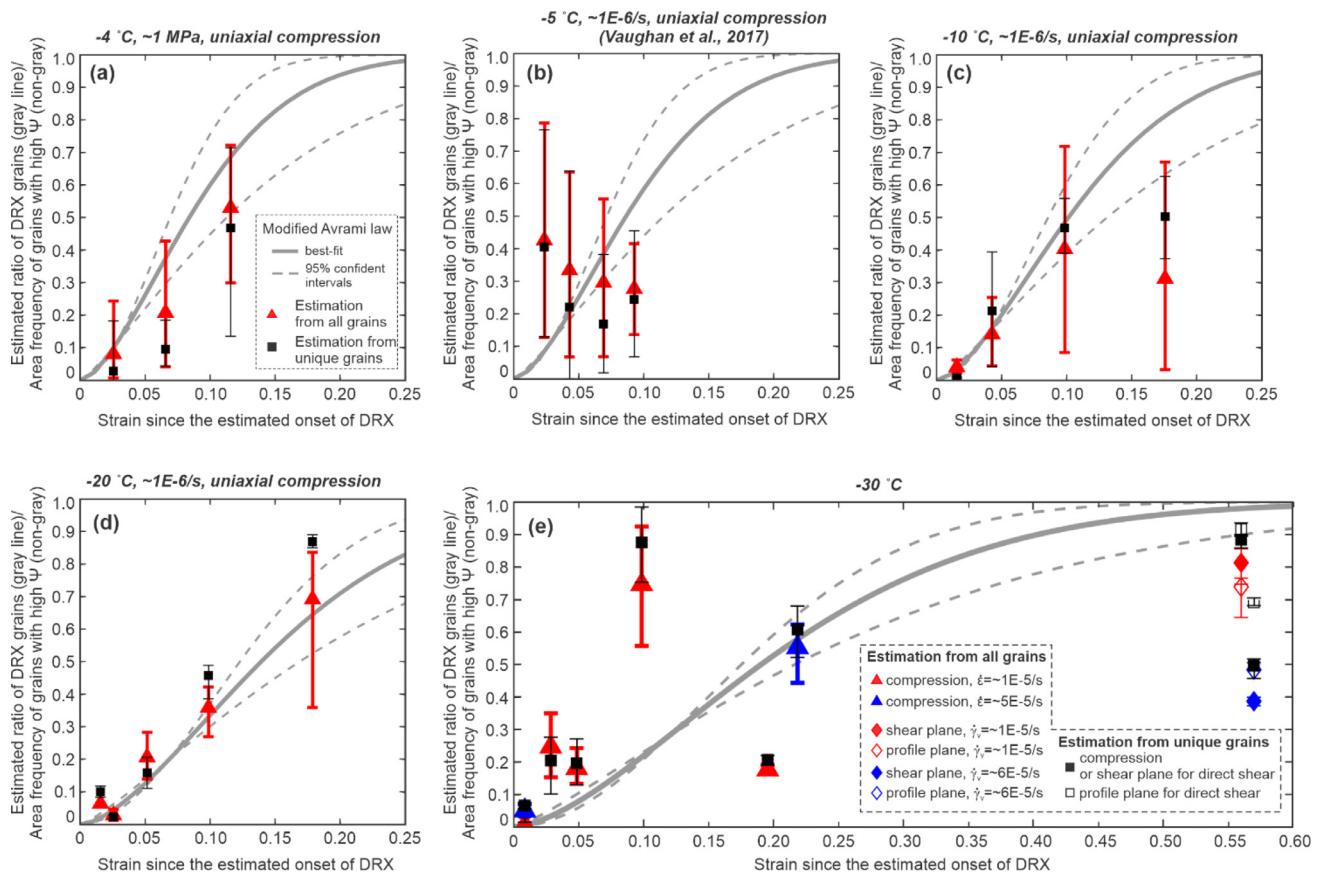


Fig. 8. Curves of estimated area frequency range of dynamically recrystallised (DRX) grains (using the modified Avrami law, Sect. 2.3) superposed by error bars representing the interval of estimated area frequency for grains with high Ψ relative to strain since the estimated onset of DRX. The data are grouped by temperatures of (a) $-4\text{ }^{\circ}\text{C}$, (b) $-5\text{ }^{\circ}\text{C}$, (c) $-10\text{ }^{\circ}\text{C}$, (d) $-20\text{ }^{\circ}\text{C}$ and (e) $-30\text{ }^{\circ}\text{C}$. Whiskers of the error bars represent limits of the interval, which are cumulative area frequencies corresponding to intersected grain sizes calculated from upper and lower bounds of linear fits for smaller and larger grains. Coloured geometrical shapes represent cumulative area frequencies corresponding to intersected grain sizes calculated from the best linear fits of smaller and larger grains using the data of all grains. Black geometrical shapes represent cumulative area frequencies corresponding to intersected grain sizes calculated from the best linear fits of smaller and larger grains using the data of unique grains. (For interpretation of the references to colour in this figure legend, the reader is referred to the web version of this article.)

interpreted as the result of strain-induced grain boundary migration (GBM) [3,9,47]. For samples deformed at fast strain rates ($\dot{\epsilon} \geq \sim 1 \times 10^{-5}\text{ s}^{-1}$), where stresses are relatively high ($\geq 2\text{ MPa}$), the number densities of distinct grains (counting 2-D grains with similar orientation as one in 3-D, Sect. 2.2.3) are greater than the starting material (Fig. 4, Tables 1, S2). This observation suggests the number of grains in 3-D increases during the deformation, and thus suggests the nucleation of new grains. Whereas grain coarsening can be facilitated by strain-induced GBM (via the consumption of grains), nucleation typically leads to grain size reduction (via the production of new, recrystallized grains that have sizes of a similar length scale as grain boundary bulges and subgrains). The data presented here—increasing grain boundary irregularity and increasing grain number density—indicate that both strain-induced GBM and nucleation were active during deformation. Similar inferences have been made for ice deformed both in the laboratory, and under natural conditions with strain rates and stresses much (one to several orders of magnitude) lower than this study [71–73]. The number density of distinct grains generally increases with strain at fast strain rates, suggesting that, under such conditions, grain nucleation outpaces grain consumption via strain-induced GBM. For samples deformed at slow strain rates ($\dot{\epsilon} = \sim 1 \times 10^{-6}\text{ s}^{-1}$), where stresses are relatively low (close to 1 MPa), the number densities of distinct grains are lower than that in the starting material, and they also generally decrease with strain (Fig. 4(a), Tables 1, S2). We explain this observation as a result of grain coarsening facilitated by GBM being more dominant than grain size reduction facilitated

by nucleation. Overall, we find a positive correlation between differential stress and the ratio between the number density of deformed samples versus the number density of the starting material (Fig. 4(b), Tables 1, S2), suggesting a relative increase in the role of nucleation with increasing stress. This hypothesis is consistent with previous studies on the steady-state grain sizes of deformed rocks and metals, which suggest that the steady-state recrystallized grain sizes should be smaller at a higher stress [74–76].

4.2. Relationships amongst grain boundary sphericity (Ψ), recrystallization processes, and deformation conditions

In general, sphericity, Ψ , decreases up to a threshold grain size, beyond which sphericity plateaus (i.e., remains constant) or decreases much more gradually. Larger grain populations (i.e., those above the grain size threshold (Sect. 3.2.3)) generally evolve towards modestly smaller sphericity values with increasing strain (Figs. 5(c-d), 6(c-d), 7(b), Sect. S4 of the supplement). In other words, larger grains become more irregular over time (and/or with increasing strain). We identify two processes that might lead to progressive increases in grain boundary irregularity for larger grains: (1) strain-induced GBM, which might facilitate grain boundaries moving away from their centres of curvature, and (2) nucleation, through which small new grains can be produced along boundaries of larger remnant grains. For smaller grains (i.e., those below the grain size threshold (Sect. 3.2.3)), sphericity decreases markedly with increasing grain size (Figs. 5(c-d), 6(c-d), 7(b), Sect.

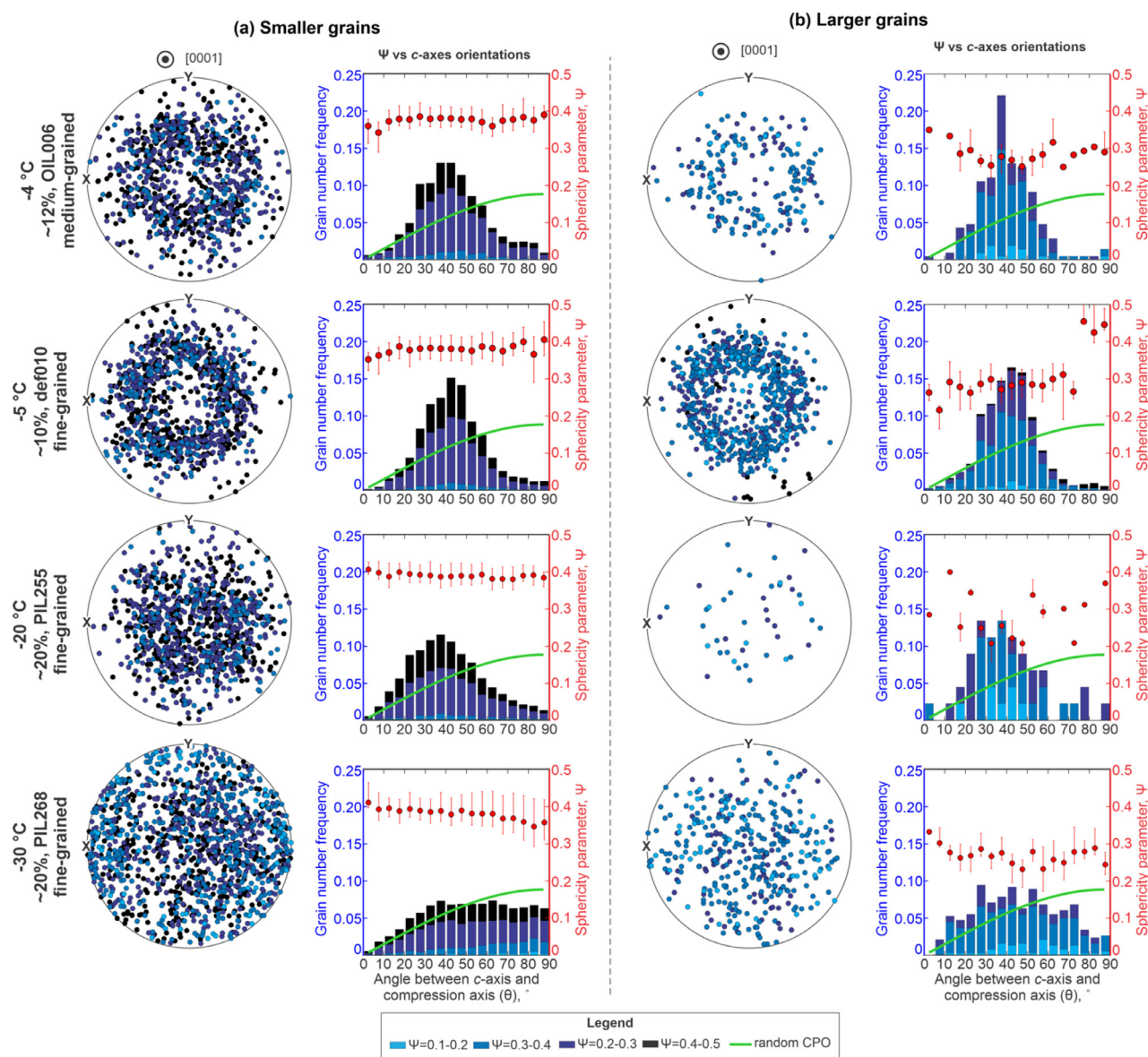


Fig. 9. Statistical analyses of sphericity parameter, Ψ , and c-axes orientations for representative ice samples deformed under a constant displacement rate ($\sim 1 \times 10^{-5} \text{ s}^{-1}$). For each sample, we present the statistics for (a) smaller grains ($< 100 \mu\text{m}$ for fine-grained ice deformed at $T \leq -10^\circ\text{C}$, and it is $< 500 \mu\text{m}$ for fine- and medium-grained ice deformed at $T > -10^\circ\text{C}$) and (b) larger grains ($> 200 \mu\text{m}$ for fine-grained ice deformed at $T \leq -10^\circ\text{C}$, and it is $> 800 \mu\text{m}$ for fine- and medium-grained ice deformed at $T > -10^\circ\text{C}$). Pole figures represent the c-axes orientations with one point per grain. Each point is coloured by the Ψ value of corresponding grain. Bar plots represent the number frequency (corresponds to the left y-axis) of grains with different Ψ as a function of angle between c-axis and compression axis, θ . The line chart, which is overlapped on bar plots, represent the number frequency of grains as a function of θ estimated from a random c-axes distribution. Error bar plots represent the IQR range (corresponds to the right y-axis) of grains with different Ψ as a function of θ . The red circle is the median point, the whiskers cover the interquartile range and represents 50% of the total data. (For interpretation of the references to colour in this figure legend, the reader is referred to the web version of this article.)

S4 of the supplement). The patterns of grain size distribution as well as sphericity for smaller grains are generally similar between all grains and unique grains (i.e., remove 2-D grains with similar orientations from all grains) (Figs. 5(c-d), 6(c-d), Sect. S4 of the supplement). Moreover, numerical modelling work from Sahagian and Proussevitch [77] shows that grain size distributions from 2-D sections are generally comparable with those from 3-D volumes, if statistically enough number of grains are captured. This number should be at least ~ 500 [78,79], which is much lower than the number of grains (for most of the samples) used in this study (Table 1). Therefore, we suggest the small grain population observed in all deformed samples are unlikely to be completely artefacts resulting from sampling limbs of large, branching grains in 2-D slices. Rock deformation studies suggest nuclei produced through subgrain rotation recrystallization should have similar sizes with

subgrains within their parent grains right after their formation [2,3,80]. Thus, discussions above suggest smaller grains observed in deformed ice samples should represent nuclei (i.e., newly recrystallized grains), statistically. These nuclei should initially have low boundary irregularity (high Ψ) that then grow by strain-induced GBM, becoming more lobate over time/strain.

It is worth noting that for those samples exhibit a bimodal grain size distribution (mostly the samples deformed at $T \leq -20^\circ\text{C}$ and to strains $> \sim 10\%$), the central minimum of the bimodal grain size distribution generally matches the threshold grain size estimated by the grain boundary sphericity statistics (e.g., PIL185, Fig. 6; PIL166, PIL268, Fig. S6; PIL243, Fig. S7). This observation suggests that statistics of grain boundary irregularity and bimodal grain size distribution should be equally efficient in identifying recrystallized grains for ice samples deformed to high strains at

low temperatures. However, most of our samples, especially the ones deformed to low strains ($< \sim 10\%$) or deformed at temperatures warmer than $-20\text{ }^\circ\text{C}$, show a unimodal grain size distribution (e.g., Figs. 5, S3, S4). Therefore, grain size distribution data will not be able to provide useful information for identifying recrystallized grains for these samples. Similarly, measures of intragranular lattice distortion—which have been used to identify recrystallized grains in rocks deformed at lower homologous temperatures [39]—are poorly suited for estimating recrystallized fractions in ice (for details see Sect. S6 of the supplement). This is probably because geometrically necessary dislocation densities are too low to generate measurable lattice curvature (using conventional EBSD with an angular resolution of nominally 1°). Thus, grain boundary irregularity should provide the most robust method for identifying recrystallized grains across experimental ice deformation conditions.

In all samples, larger grains undergo a modest decrease in sphericity with increasing strain/time, regardless of temperature. However, the slope of the data in sphericity – grain size is temperature dependant. At lower temperatures ($T < -10\text{ }^\circ\text{C}$), we observe a “plateau” in sphericity – grain size for larger grains, such that sphericity values are similar across different grain sizes, and at all strains up to $\sim 60\%$ (Figs. 6(d), 7(b), Sect. S4 of the supplement). We suggest that, at lower temperatures, the “plateau” of Ψ represents the population of remnant grains, that all started off with similar shapes (moderate Ψ) and became more lobate with increasing strain/time (reducing Ψ). If this is correct, then the change in slope of sphericity – grain size at intermediate grain sizes represents the change from (small) grains that have nucleated and grown by GBM during the experiment, to (large) grains that were present in the starting material. At higher temperatures ($T \geq -10\text{ }^\circ\text{C}$), Ψ decreases modestly above the grain size threshold, but the slope of these sphericity – grain size data is shallower than that within the smaller grain size category (Figs. 5(d), 7(b), Sect. S4 of the supplement). We discuss this observation later, in Section 4.3.

4.3. Using sphericity data to quantify grain boundary migration rates

We interpret the threshold grain size corresponding to the change in slope on the sphericity – grain size graph as the largest grain size that a recrystallized nucleus has grown to by the end of each experiment (Sect. 4.2). This hypothesis is supported by the observation showing area frequency of recrystallized grains estimated from sphericity data is generally comparable with that estimated by the global dynamic recrystallization model, for samples deformed in this study (Figs. 8(a), 8(c-e); Sect. 3.2.4). By assuming that the smallest nuclei formed at the onset of dynamic recrystallization and grew to the threshold grain size over the duration of a given experiment, we can calculate the rate of grain growth (Fig. 10). From the next paragraph, we will calculate grain growth rates based on the changes in grain area, grain radius, and grain perimeter.

Rates of change of area (\dot{A}), radius (\dot{r}), and perimeter (\dot{P}) are calculated from differences between the minimum (i.e., initial) and maximum (i.e., final) area, area-equivalent radius, and perimeter, respectively, divided by the estimated time during which GBM is active, t . We calculate t from the duration of each experiment, minus the time required to reach a critical strain for the onset of dynamic recrystallization. For various crystalline materials, dynamic recrystallization begins at 40–95% of the strain at peak stress (in constant rate experiments) or minimum strain rate (in constant load experiments) [68,81], with a typical value of $0.71\varepsilon_p$ [48] that we adopt here, where ε_p is the strain at peak stress. Lower, best-fit, and upper bounds on the initial (i.e., minimum) grain area, area-equivalent radius, and grain perimeter are given by assuming that perfectly spherical ($\Psi = 0.5$) nuclei form with area-equivalent diameters of 20, 50 or $100\text{ }\mu\text{m}$, respectively. These grain

sizes are based on subgrain size statistics reported in [9], which used part of the EBSD data presented in this study (-10 , -20 and $-30\text{ }^\circ\text{C}$, $\sim 1 \times 10^{-5}\text{ s}^{-1}$). Best-fit final (i.e., maximum) grain area, area-equivalent radius, and grain perimeter, are based on the best-fit threshold grain sizes within sphericity – grain size graph (Sect. 3.2.4). Lower and upper bounds on the final (i.e., maximum) grain area and area-equivalent radius are given by the uncertainties in the threshold grain sizes within Ψ -grain size plots (Sect. 3.2.4). Meanwhile, lower and upper bounds on final (i.e., maximum) area-equivalent perimeter are calculated by assuming that recrystallized grains remain either perfectly spherical ($\Psi_{\text{spherical}} = 0.5$) or become highly lobate ($\Psi_{\text{lobate}} = 0.1$) by the end of an experiment. The upper bound on area-equivalent perimeter, P_{lobate} , is related to the lower bound on area-equivalent perimeter, $P_{\text{spherical}}$, as follows (transformed from Eq. (1)):

$$P_{\text{lobate}} = \frac{\Psi_{\text{spherical}}}{\Psi_{\text{lobate}}} \times P_{\text{spherical}}. \quad (3)$$

There is no significant difference in the values of \dot{A} , \dot{r} and \dot{P} estimated using the lower, upper, and best-fit measurements of grain area, equivalent radius, and perimeter (Sect. S7 of the supplement). Therefore, we present the data calculated from the best fit threshold grain size with the initial recrystallized grain size of $50\text{ }\mu\text{m}$. Deformed samples have similar values of \dot{A} , \dot{r} and \dot{P} at different temperatures (Fig. 10). One way to explain this observation is the rate of GBM, V , depends on two parameters; the boundary mobility, M , and the driving force, P (Eq. (4)) [4].

$$V = MP \quad (4)$$

Grain boundary mobility, M , obeys and Arrhenius type relationship with the following form [4,82]:

$$M = M_0 \exp\left(-\frac{Q}{RT}\right), \quad (5)$$

where Q is the apparent activation energy, which may be related to the atom-scale, thermally activated, rate-limiting process that controls boundary migration, R is the gas constant, T is the temperature in Kelvin. Eq. (5) suggests grain boundary mobility should increase exponentially with increasing temperature.

The driving force for grain boundary migration, P , is provided mostly by grain-to-grain variations in dislocation density, expressed as [83]:

$$P = \mu b^2 \Delta\rho, \quad (6)$$

where μ is the shear modulus, b is the modulus of the Burgers vector and $\Delta\rho$ is the difference of dislocation density across a given grain boundary segment. The $\Delta\rho$ is likely to have a positive correlation with stress [84,85]. Eq. (6) suggests the driving force provided by strain energy should be greater at higher stresses (and lower temperatures under similar strain rates), where dislocation density differences are greater. Thus, in principle, the product of mobility and driving force may be nearly constant over a narrow range of temperature. We attempt to quantify this in the next few paragraphs.

Grain boundary mobility is a function of temperature, which can be quantified by a kinetic constant, k (m^2/s) [82,86,87]. The k derived for normal grain growth of bubble-free pure water ice from Azuma and others [82] can be written as:

$$k = 2sM\gamma_b, \quad (7)$$

where s is a constant of the order of one and γ_b is grain boundary energy, which is independent of grain size [82,88]. Eq. (7) suggests that the k values should be a measure of grain boundary mobility, M , but not the velocity of GBM under normal grain growth. Values of $\log(k)$ derived for normal grain growth of bubble-free pure water ice [82] and polar firn (summarized by Paterson [89]) follows an Arrhenius temperature dependence (Fig. 11(a)). We have

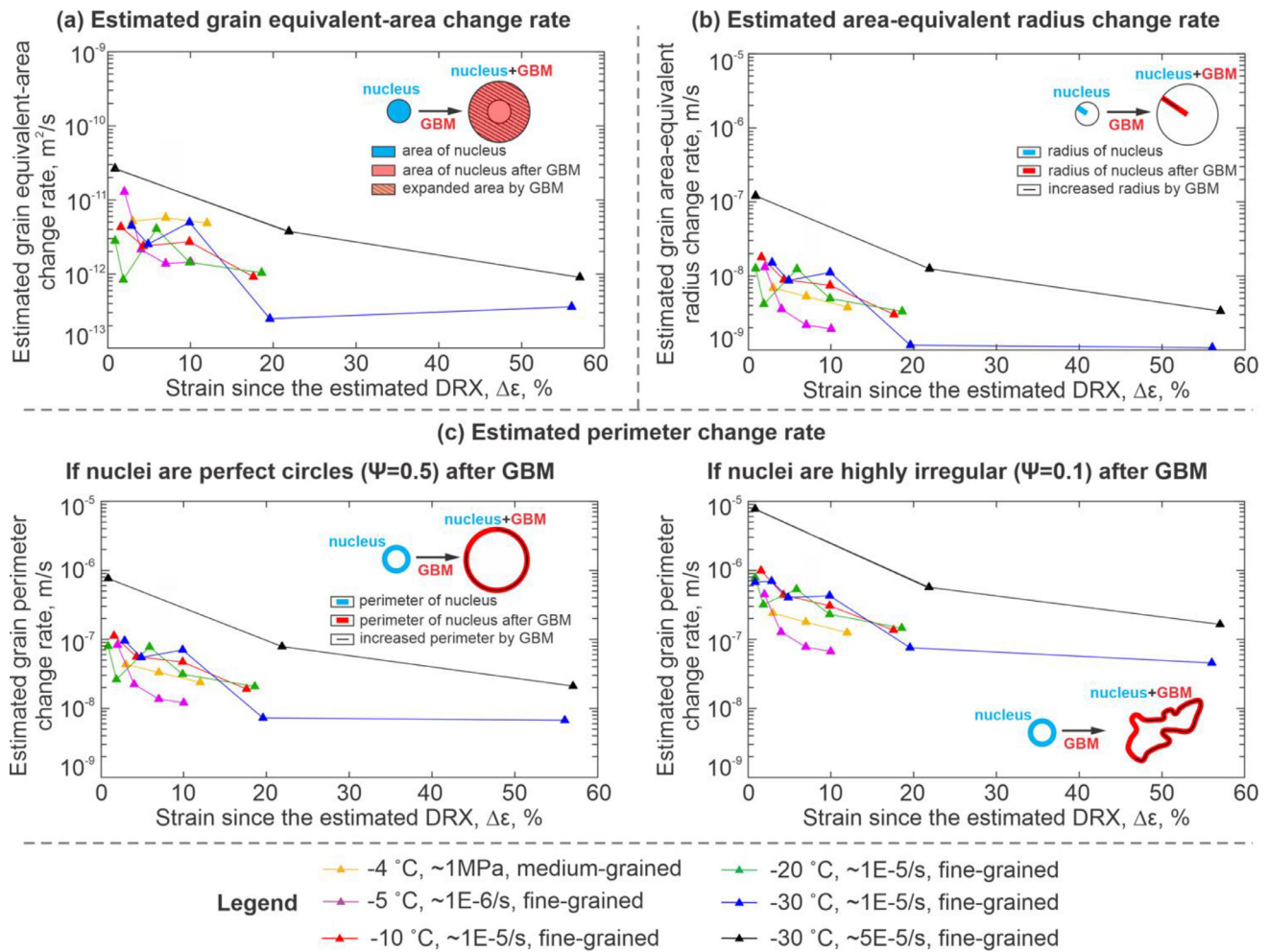


Fig. 10. Estimated upper limit of change rate of (a) grain area, (b) area-equivalent radius and (c) area-equivalent perimeter as a function of strain since the estimated onset of dynamic recrystallization (Sect. 4.3).

plotted our grain area change rates on the same Arrhenius plot used to show k values for normal grain growth data (Fig. 11(a)). The relative magnitudes of the growth rates and the k values are arbitrary, but the plot illustrates that our dynamic grain growth data do not match the Arrhenius relationship of the normal grain growth data—dynamic grain growth appears to be much less temperature dependant.

Previous studies have shown that boundary mobility can be controlled by boundary misorientation [4]. (Low-angle) subgrain boundaries generally show a higher boundary velocity and mobility, as well as a greater activation energy for migration at higher misorientation angles. However, compared with subgrain boundaries, the velocity, mobility, and the activation energy for high angle grain boundary migration are much less misorientation dependant (Figs. 5.6, 5.7, 5.13 from [4]). Furthermore, in materials with a large dependence of boundary migration rate on boundary misorientation, e.g., materials with second phases or with limited sample thickness (film-shaped sample), abnormal grain growth is often observed [90–92]. We do not find any evidence of abnormal grain growth as an important process in ice—no abnormally large grains are observed in the pure water ice samples deformed in this study, and samples deformed to progressively higher strains at the same temperature generally show similar change rates in grain area, area-equivalent radius and perimeter without any abrupt fluctuations (Fig. 10). Therefore, we suggest GBM should be mainly driven

by surface energy and strain energy, with little dependence on boundary misorientation, for ice samples deformed in this study.

There is no intrinsic reason to believe that the mobility of boundaries under normal grain growth driven by surface energy is different to the mobility of boundaries driven by strain energy at the same temperature. If so, we can use the ratio of grain area change, \dot{A} , and the normal grain growth kinetic constant, k , at a particular temperature to quantify the relative difference in grain growth driving force at that temperature—this difference directly represents the difference in driving force, ΔP , due to strain energy. The relative driving force, ΔP , can be quantified by $\frac{\dot{A}}{k_{Azuma}}$, where k_{Azuma} is the best fit kinematic constant from Azuma and others [82], because \dot{A} and k_{Azuma} are functions of V and M , respectively Eqs. (4), ((7)).

Fig. 11(b) shows $\frac{\dot{A}}{k_{Azuma}}$ generally increases with bulk differential stress, suggesting a positive relation between stress and driving force. Samples deformed under similar conditions show $\frac{\dot{A}}{k_{Azuma}}$ generally decreases as the strain increases from ~3%, consistent with a reduction of stress with an increasing strain after peak stress. Moreover, under similar strain rates, stress generally increases with a decreasing temperature (Fig. 11(b)), suggesting driving force should increase with decreasing temperature. One way to explain these data is driving force should be dominated by strain energy (Eq. (6)). Strain energy is a function of dislocation den-

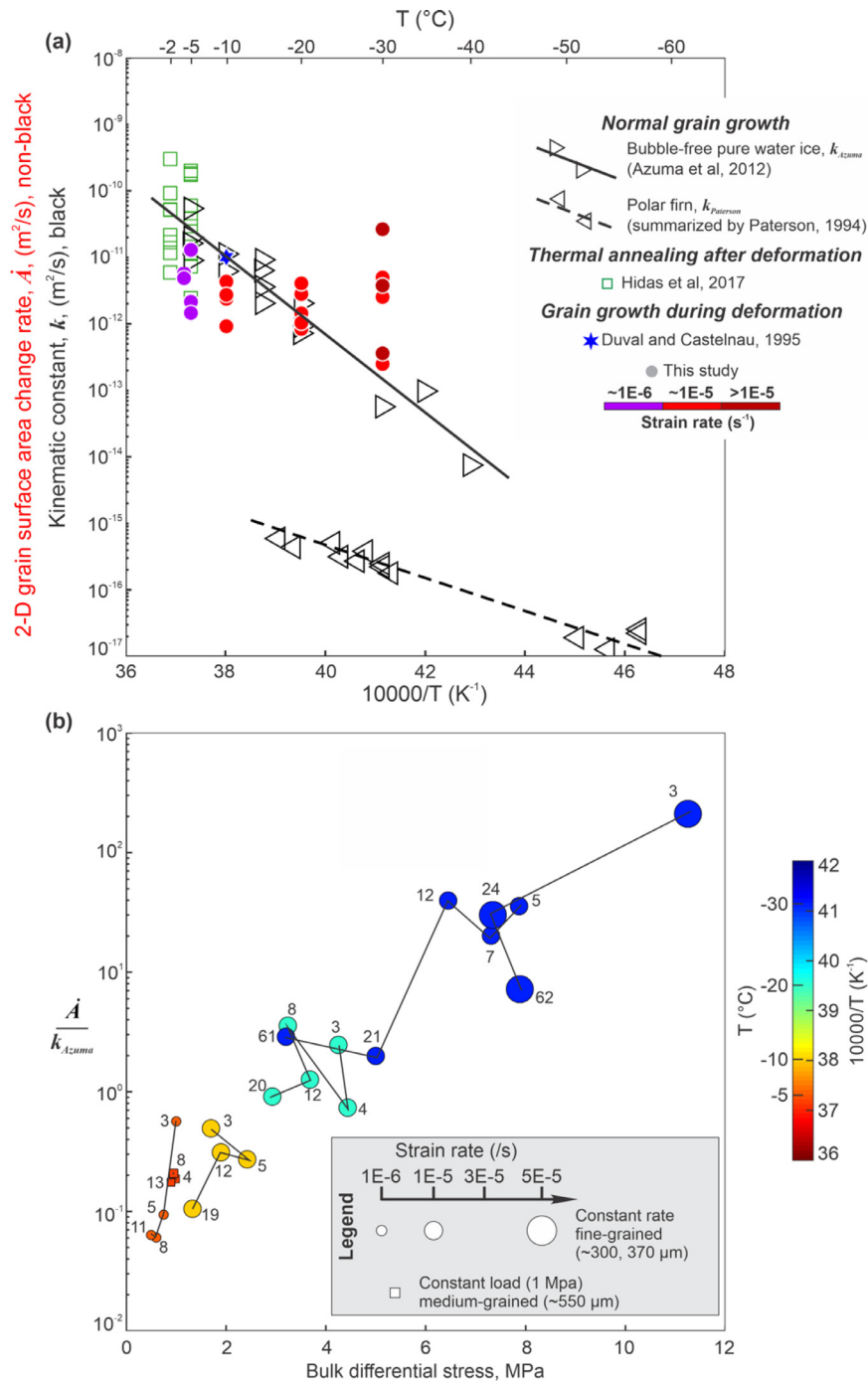


Fig. 11. (a) Arrhenius plot of kinetic constant, k , for normal grain growth, and 2-D grain surface area change, \dot{A} , calculated for our data. The k is for normal grain growth of bubble-free pure water ice [82] and polar firn [89]. Data of 2-D grain surface area change are taken from this study (Section 4.3) and ice that deformed at -7°C and then annealed at -2 and -5°C [59]. (b) Scatter plot of $\frac{\dot{A}}{k_{\text{Azuma}}}$ as a function of bulk differential stress, where k_{Azuma} is the best fit kinetic constant from [82] for the same temperature as a measure of \dot{A} from this study. Samples deformed at similar temperature and strain rate/stress are connected by dashed lines. The number next to each point represents the equivalent strain (%), i.e., true axial strain for uniaxial compression; von Mises strain for direct shear.

sity difference, and should increase with stress [84,85]. On the other hand, grain boundary mobility decreases with a decreasing temperature (Eq. (5)), but grain area change rates, \dot{A} , measured from deformed ice (this study; [59]) remains similar at low and high temperatures (Fig. 10(a), 11(a)). These data suggest that, under similar strain rates, decreasing temperature correlates with (1) a decreasing grain boundary mobility, and (2) an increasing strain energy that leads to an increasing driving force. The balance between decreasing boundary mobility and an increasing driving

force is likely result in similar GBM rates between high and low temperatures (Eq. (4)).

At low temperatures sphericity is constant in larger grains, whereas at higher temperatures there is a slight reduction in sphericity with increasing size in the larger grains (Sect. 4.2). A potential explanation for this is in the relative balance of strain energy and surface energy driving forces. Boundaries become more irregular during dynamic recrystallization, probably facilitated by strain-induced GBM and nucleation, as a consequence of hetero-

geneties in driving force and/or mobility (Sect. 4.2). The surface energy driving force, in contrast, will drive the decrease in boundary irregularity to minimize the total surface area per volume (equivalent to curvature) of boundaries [3,4]. The surface energy component should be independent of temperature, but strain energy should increase with a decreasing temperature. Therefore, at higher temperatures surface energy should be a more significant component than at low temperature compared with strain energy. The driving force provided by surface energy has an inverse relationship with grain size [82]. Therefore, surface energy should provide a larger driving force of GBM for smaller grains and it should lead to a more significant reduction in boundary irregularity (increase sphericity) for these smaller grains.

4.4. Grain boundary migration and grain orientation

Grains with different *c*-axes orientations generally have similar Ψ values (e.g., Fig. 9, Sect. S5 of the supplement), suggesting that crystallographic preferred orientation (CPO) has no obvious control on the development rate of grain boundary irregularity, which is likely controlled by the balance between strain-induced GBM and nucleation (Sect. 4.2). For ice samples deformed at very high temperatures (-4 and -5 °C), GBM is more dominant than nucleation (Sect. 4.1), and similar Ψ values for grains with different *c*-axes orientations probably mean that CPO has a weak control on the rate of strain-induced GBM. Initially this seems problematic, as we understand that strain-induced GBM favours the growth of easy slip grains (i.e., those with high Schmid factors, orientated with their *c*-axes at $40 - 50^\circ$ from the compression axis) at the expense of hard slip grains [47,53]. Since the boundaries of easy slip grains should preferentially migrate towards hard slip grains, it would seem logical for easy slip grains to become more lobate through this process. In reality, however, the boundaries of both types of grains will become lobate at the same rate. It is therefore quite possible for strain-induced GBM to favour the growth of grains in particular orientations without the boundaries of those grains becoming more irregular than the boundaries of the grains being consumed.

5. Conclusions

- 1 Polycrystalline pure water ice samples were deformed to progressively higher strains under uniaxial compression or direct shear at temperatures of -4 to -30 °C. Samples deformed to strains higher than $\sim 3\%$ are characterised by grains with irregular boundaries, indicating a possibly branching grain shape in 3-D, which is likely a result of strain-induced GBM. The number density (number of grains per unit area) of distinct grains, i.e., counting nearby 2-D grains with similar orientations as one grain in 3-D, increases with strain at high stresses; but it decreases with strain at low stresses. This observation suggests the relative activity between strain-induced GBM, which reduces the total grain number, and nucleation, which increases the total grain number, is a function of stress. The number density of distinct grains is higher at a higher stress, suggesting a more active nucleation.
- 2 We applied a grain size insensitive sphericity parameter, Ψ , to quantify the boundary irregularity. A higher Ψ corresponds to a lower boundary irregularity. Deformed samples show Ψ decreases with grain size up to a threshold grain size, above which Ψ remains stable (-20 and -30 °C) or decreases slightly with grain size (-4 , -5 and -10 °C). We interpret the decrease of Ψ from the smallest grain size to the threshold grain size as relating to nuclei, which initially have the smallest size and low boundary irregularity, that grow by strain-induced GBM with boundaries becoming more irregular. We suggest that, at low

temperatures, the stable Ψ above the threshold grain size represent original grains, which initially have similar low irregularities and become more lobate at similar rates due to strain-induced GBM and nucleation. At high temperatures, a reduction of strain energy leads to a relatively greater contribution of surface energy to the driving force of GBM. The driving force provided by surface energy is grain size sensitive, and it is responsible for greater reduction of boundary irregularity within smaller grains.

- 3 Threshold grain sizes are considered as the largest grain sizes that nuclei have grown into at the end of experiments. We used the threshold grain size and experimental time to calculate rates of recrystallization and average grain size change that are associated with GBM. Grain size change rates are similar between low and high temperatures, suggesting similar GBM rates. We suggest the similar GBM rate can be explained by a balance between grain boundary mobility and driving force. Because grain boundary mobility decreases with a decreasing temperature, as quantified by previous studies. Data from this study show driving force has a positive correlation with stress, and it is higher at a lower temperature under a constant strain rate.
- 4 Grains with different *c*-axes orientations generally have similar sphericities. At very high temperatures (-4 and -5 °C), where GBM dominates deformation, these data suggest little correlation between the CPO and GBM rate. This hypothesis does not preclude favored growth of particular orientations at the boundary between grains that are growing and being consumed.

Data availability

Data can be obtained via <https://doi.org/10.6084/m9.figshare.13456550> (Fan et al., 2020).

Declaration of Competing Interest

The authors declare that they have no known competing financial interests or personal relationships that could have appeared to influence the work reported in this paper.

Acknowledgements

We are thankful to Pat Langhorne for providing the cold-room facility at University of Otago. This work was supported by a NASA fund (grant no. NNX15AM69G) to David L. Goldsby and two Marsden Funds of the Royal Society of New Zealand (grant nos. U001116, U00052) to David J. Prior. Sheng Fan was supported by the University of Otago doctoral scholarship and the Antarctica New Zealand doctoral scholarship.

Supplementary materials

Supplementary material associated with this article can be found, in the online version, at doi:10.1016/j.actamat.2021.116810.

Appendix A. Influence of EBSD step size on sphericity parameter statistics

With increasing EBSD step size, grain boundaries appear increasingly pixelated, and small grain boundary features (e.g., bulges) become undetectable. To investigate how step size influences grain boundary irregularity measurements, we performed sensitivity tests of EBSD data of fine-grained ice samples (~ 300 μm) deformed at -20 °C, with a step size of 5 μm . In the

test, we artificially increased the step size of the EBSD data to 10, 20, 30 and 40 μm by selecting every second, fourth, sixth and eighth pixel, respectively, from each row and column of the EBSD pixel data. Ice grains were reconstructed with a grain boundary threshold of 10° , and grains with area equivalent diameter larger than 20 μm were removed.

We use PIL185 (-20°C , $\sim 12\%$ strain) as an example to illustrate the change of microstructural statistics while step size increases (Figs. A.1(a-d)). For a large individual grain, grain boundary features resolved at the EBSD step size of 5 μm are mostly preserved up to a step size of 30 μm ; grain boundary sphericity remains relatively similar between step sizes of 5 and 30 μm (Fig. A.1(a)). As

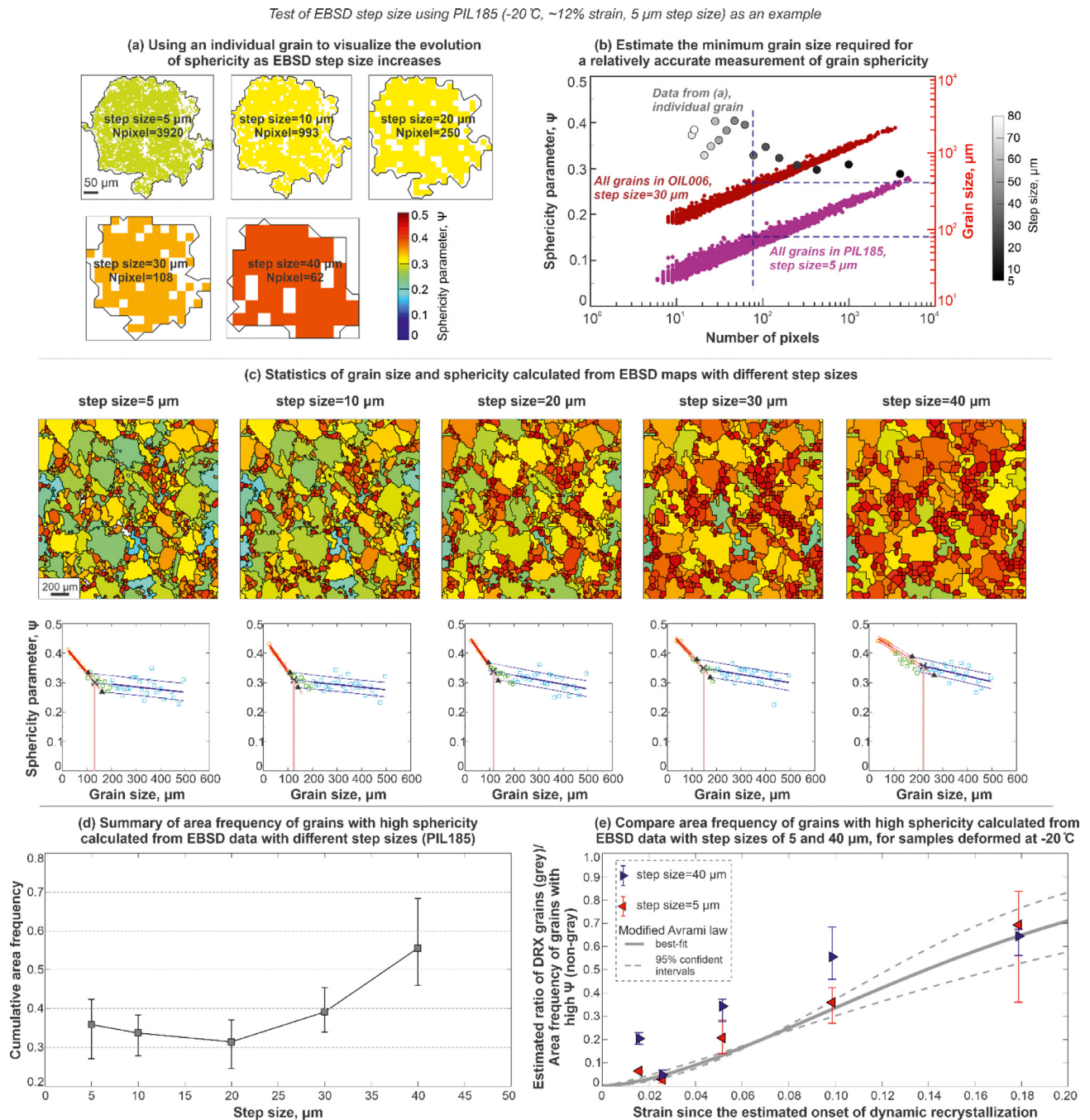


Fig. A.1. Testing the impact of EBSD step size on the statistics of sphericity parameter. **(a)** Using an individual grain with a relatively large number of pixels from sample PIL185 (-20°C , $\sim 12\%$ strain) to illustrate the evolution of grain boundary sphericity, Ψ , as the EBSD step size increases from 5 μm . **(b)** The scatter plot with grey dots represents the Ψ as a function pixel number corresponding to the individual grain (presented in (a)) with the EBSD step size artificially increased from 5 to 80 μm . The scatter plot with pink and dark red dots represents the grain size as a function of pixel number corresponding to all grains in PIL185 (EBSD step size of 5 μm) and OIL006 (EBSD step size of 30 μm), respectively. The blue dashed lines highlight the grain size required for a grain to contain ~ 100 pixels, at EBSD step sizes of 5 and 30 μm . **(c)** Analyses of sphericity parameters and grain sizes for sample PIL185 with the EBSD step size of 5, 10, 20, 30 and 40 μm . Microstructural maps (**row 1**) show grains each grain coloured by corresponding sphericity parameter, Ψ . Linear fits were applied on the median Ψ -grain size data for smaller ($< 100 \mu\text{m}$) and larger grains ($> 200 \mu\text{m}$), separately (**row 2**). Linear fit intersections of best fits between smaller and larger grain data are marked as cross marks. The best-fit grain size is marked with thick pink vertical line. **(d)** Summary of area frequency metrics of grains with high Ψ calculated from the EBSD data with different step sizes corresponding to (c). **(e)** Comparison of area frequency metrics of grains with high Ψ calculated from the EBSD data with step sizes of 5 and 40 μm , for samples deformed at -20°C . (For interpretation of the references to colour in this figure legend, the reader is referred to the web version of this article.)

the step size increases to 40 μm or higher, grain boundary sphericity increases drastically due to a significant loss of grain boundary resolution (Figs. A.1 (a-b)). These observations suggest, for individual grains, EBSD maps with step sizes of 5 – 30 μm can preserve grain boundary features with similar accuracies; the grain boundary features acquired at step sizes larger than 40 μm are less accurate. From these data, we can also estimate at least how many pixels are required for a grain to have a relative accurate grain boundary irregularity measurement: for an individual grain, the grain boundary sphericity, Ψ , remains similar before the number of pixels per grain reduces to 100; the Ψ increases drastically when a grain contains fewer than 100 (grey dots in Fig. A.1(b)). The grain size has a positive correlation with the number of pixels (red dots, Fig. A.1(b)), and grains with grain sizes larger than $\sim 80\mu\text{m}$ and $\sim 400\mu\text{m}$ generally have more than 100 pixels at step sizes of 5 μm and 30 μm , respectively (indicated by blue dashed line, Fig. A.1(b)). These data suggest that grains with grain sizes smaller than $\sim 80\mu\text{m}$ and 400 μm at EBSD step sizes of 5 μm and 30 μm , respectively, should have relatively less accurate grain boundary irregularity measurements. However, if we reduce the resolution, i.e., increase the step size, for the whole EBSD map, the pattern of grain boundary sphericity as a function of grain size remains similar between small and large step sizes (e.g., Fig. A.1(c)). These observations suggest that even though we are less likely to acquire a true measurement of sphericity in small grains, we can be fairly certain that the sphericity – grain size trends are real, i.e., they are not an artefact of step size.

For an entire EBSD map, the sphericity of larger grains is generally higher at the step sizes of 30 and 40 μm than at step sizes smaller than 30 μm (e.g., Fig. A.1(c)). The threshold grain sizes as well as area frequencies of grains with high sphericities are similar for data with step sizes of 5, 10, 20 and 30 μm , and they are lower than at a step size of 40 μm (e.g., Fig. A.1(d)). For all samples deformed at $-20\text{ }^\circ\text{C}$, differences in the area frequency of grains with high sphericity between high and low strains becomes less significant at a step size of 40 μm than at a step size of 5 μm (Fig. A.1(e)). These observations suggest that EBSD data with a coarser step size (40 μm in the test) are more prone to errors in estimating the frequency of recrystallized grains compared with EBSD data collected at a finer step size.

Appendix B. Influence of grain boundary smoothing on sphericity parameter statistics

In the MTEX toolbox environment, boundaries comprise individual elements drawn between pixels with misorientation angles larger than 10° . Due to the square shape of pixels (prescribed by

Oxford Instruments software), boundary elements lie either vertically or horizontally within the plane of analysis (Fig. B.1(a)). Grains containing fewer pixels (i.e., smaller grains in maps with a fixed step size) appear more pixelated than grains containing numerous pixels. MTEX allows us to reduce artificial pixelation of grain boundary elements by applying a *smooth* function, which enhances the overall grain boundary smoothness by interpolating the coordinates of grain boundary elements while triple junction points remain locked (highlighted by pink circles in Fig. B.1(a)). We varied a grain boundary smooth parameter, X , in the *smooth* function, to systematically control the magnitude of grain boundary smoothing; a higher X value corresponds to an enhancement in grain boundary smoothing (Figs. B.1(a-b)).

We use PIL166 ($-30\text{ }^\circ\text{C}$, $\sim 12\%$ strain) as an example to illustrate the statistical effects of grain boundary smoothing (Figs. B.1(a-d)). Grains with a relatively large number of pixels should have a more accurate grain boundary sphericity measurement (Appendix A). For grains containing more than 2000 pixels, the sphericity parameter, Ψ , increases gradually as X increases and grain boundary features are progressively removed (Fig. B.1(b)). Given the gradual increase in sphericity with increasing X , it is difficult to identify an optimal degree of grain boundary smoothing, X . Instead, we can find the ideal amount of smoothing by analysing an undeformed sample—in a raw, unsmoothed EBSD map, the boundary segments have a high variance in grain boundary azimuths (since most boundaries are aligned with the x and y axes), producing an uneven rose diagram (Fig. B.1(e)). However, undeformed ice samples should have a uniform grain structure and therefore a relatively even number of grain boundary segments in all directions. We find that an even distribution of grain boundary azimuths is approached at $X=3-5$ (Figs. B.1(e-f)). Thus, $X=3-5$ provides the optimal amount of smoothing, by reducing pixelation while retaining real grain boundary features.

We compare the sphericity statistics of grains with smoothed boundaries, Ψ_s , and grains without smoothed boundaries, Ψ_o , at grain boundary smooth parameter, X , values of 3 and 5, for deformed samples (Figs. B.1(c), full data shown in Sect. S8 of the supplement). The difference between Ψ_s and Ψ_o is greater for smaller grains, but it is generally insignificant for both of smaller and larger grains (Fig. B.1(c), Sect. S8 of the supplement). Moreover, the intersection grain sizes of grains with high sphericities are generally similar between unsmoothed data and smoothed data with X of 3 and 5 (Fig. B.1(d), Sect. S8 of the supplement), although unsmoothed grain boundaries appear to slightly underestimate the true sphericity of individual grains. Overall, however, grain boundary smoothing has little effect on the grain boundary irregularity statistics.

Test of grain boundary smoothing using PIL166 ($-30\text{ }^{\circ}\text{C}$, $\sim 12\%$ strain, $5\text{ }\mu\text{m}$ step size) as an example

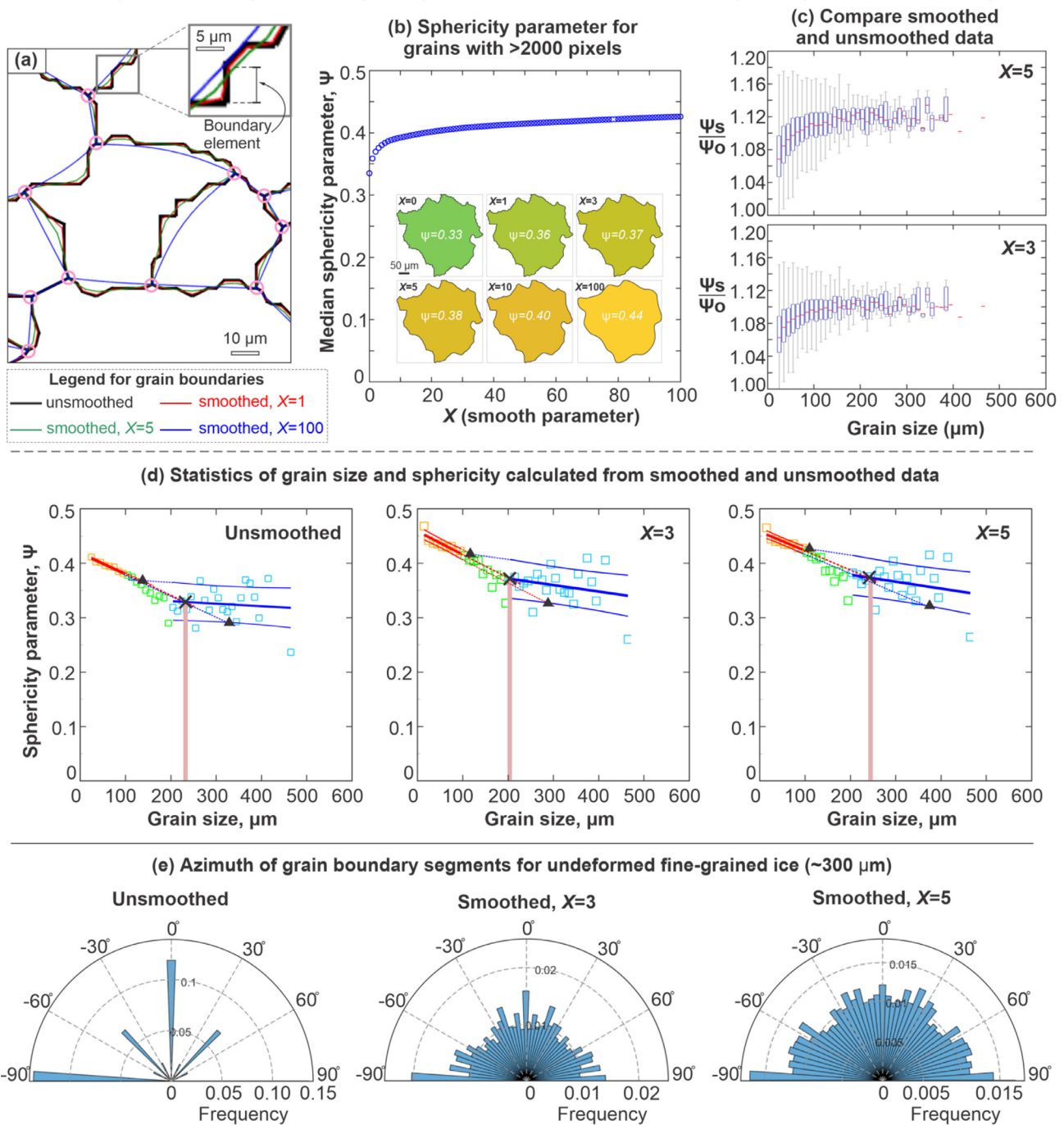


Fig. B.1. Testing the impact of grain boundary smoothing on the statistics of sphericity parameter. **(a)** Illustration of the *smooth* function from MTEX that can be applied to enhance the overall grain boundary smoothness using a subarea of the EBSD map from PIL166 ($-30\text{ }^{\circ}\text{C}$, $\sim 12\%$ strain) as an example. The *smooth* function can interpolate the coordinates of grain boundary elements while the triple junction points (marked by pink circles) remain locked. The intensity of boundary smoothing is controlled by a smooth parameter, X . **(b)** The scatter plot with blue circles shows the evolution of median sphericity parameter, Ψ , values calculated from grains containing more than 2000 pixels as boundaries of these grains become progressively smoothed (controlled by the smooth parameter, X). We present an example grain to illustrate the change of Ψ values as X increases. The grain is coloured by Ψ (legend in Fig. A.1(a)). **(c)** A comparison of the sphericity parameter statistics calculated from grains with smoothed boundaries, Ψ_s (with smooth parameter, X , of 3 and 5), and grains without smoothed boundaries, Ψ_o , using PIL166 as an example. Error bar plots represent the IQR range of the ratio between Ψ_s and Ψ_o as a function of grain size. The red line is the median point, the blue box covers the interquartile range and represents 50% of the total data, the whiskers are the extremes. **(d)** Linear fits on the median sphericity – grain size statistics for the EBSD data of sample PIL166 without smoothed grain boundaries and data with smoothed grain boundaries (X of 3 and 5). Linear fits comprise the best linear fit (thick lines) and upper and lower bound of linear fit, i.e., best linear fit $\pm 95\%$ standard error (thin lines). Linear fit intersections of upper bounds of the linear fits and lower bound of the linear fits between smaller and larger grain data are marked as triangles. Linear fit intersections of best fits between smaller and larger grain data are marked with cross marks. The best-fit grain size is marked with thick pink vertical line. **(e)** Rose diagrams showing the evolution of azimuths of grain boundary segments for undeformed fine-grained ice ($\sim 300\text{ }\mu\text{m}$) as the grain boundary smoothing becomes enhanced (X of 0, 3 and 5).

References

- [1] B. Kamb, Experimental Recrystallization of Ice Under Stress, in: *Flow Fract. Rocks*, American Geophysical Union, 1972, pp. 211–241, doi:[10.1029/GM016p0211](https://doi.org/10.1029/GM016p0211).
- [2] S. White, The Effects of Strain on the Microstructures, Fabrics, and Deformation Mechanisms in Quartzites, *Philos. Trans. R. Soc. A Math. Phys. Sci.* 283 (1976) 69–86 <https://www.jstor.org/stable/74630>.
- [3] J.L. Urai, W.D. Means, G.S. Lister, in: *Dynamic Recrystallization of Minerals*, Miner. Rock Deform. Lab. Stud., 1986, pp. 161–199, doi:[10.1029/GM036p0161](https://doi.org/10.1029/GM036p0161).
- [4] F.J. Humphreys, M. Hatherly, A. Rollett, *Recrystallization and Related Annealing Phenomena*, Third, Elsevier Ltd., 2017.
- [5] W.D. Means, Microstructure and micromotion in recrystallization flow of octachloropropane: a first look, *Geol. Rundschau*. 72 (1983) 511–528, doi:[10.1007/BF01822080](https://doi.org/10.1007/BF01822080).
- [6] G. Hirth, D.L. Kohlstedt, Experimental constraints on the dynamics of the partially molten upper mantle: 2. Deformation in the dislocation creep regime, *J. Geophys. Res. Solid Earth*. 100 (1995) 15441–15449, doi:[10.1029/95JB01292](https://doi.org/10.1029/95JB01292).
- [7] M. Montagnat, T. Chauve, F. Barou, A. Tommasi, B. Beausir, C. Fressengeas, Analysis of Dynamic Recrystallization of Ice from EBSD Orientation Mapping, *Front. Earth Sci.* 3 (2015) 411–413, doi:[10.3389/feart.2015.00081](https://doi.org/10.3389/feart.2015.00081).
- [8] C. Qi, D.L. Goldsby, D.J. Prior, The down-stress transition from cluster to cone fabrics in experimentally deformed ice, *Earth Planet. Sci. Lett.* 471 (2017) 136–147, doi:[10.1016/j.epsl.2017.05.008](https://doi.org/10.1016/j.epsl.2017.05.008).
- [9] S. Fan, T.F. Hager, D.J. Prior, A.J. Cross, D.L. Goldsby, C. Qi, M. Negrini, J. Wheeler, Temperature and strain controls on ice deformation mechanisms: insights from the microstructures of samples deformed to progressively higher strains at -10 , -20 and -30 °C, *Cryosph* 14 (2020) 3875–3905, doi:[10.5194/tc-14-3875-2020](https://doi.org/10.5194/tc-14-3875-2020).
- [10] J.E. Bailey, P.B. Hirsch, The recrystallization process in some polycrystalline metals, *Proc. R. Soc. London. Ser. A. Math. Phys. Sci.* 267 (1962) 11–30, doi:[10.1098/rspa.1962.0080](https://doi.org/10.1098/rspa.1962.0080).
- [11] A. Halfpenny, D.J. Prior, J. Wheeler, Analysis of dynamic recrystallization and nucleation in a quartzite mylonite, *Tectonophysics* 427 (2006) 3–14, doi:[10.1016/j.tecto.2006.05.016](https://doi.org/10.1016/j.tecto.2006.05.016).
- [12] J.M. Burgers, Geometrical considerations concerning the structural irregularities to be assumed in a crystal, *Proc. Phys. Soc.* 52 (1940) 23–33, doi:[10.1088/0959-5309/52/1/304](https://doi.org/10.1088/0959-5309/52/1/304).
- [13] J.A. Tullis, High temperature deformation of rocks and minerals, *Rev. Geophys.* 17 (1979) 1137–1154, doi:[10.1029/RC017i006p01137](https://doi.org/10.1029/RC017i006p01137).
- [14] M. Stipp, H. Stünitz, R. Heilbronner, S.M. Schmid, The eastern Tonale fault zone: a “natural laboratory” for crystal plastic deformation of quartz over a temperature range from 250 to 700 °C, *J. Struct. Geol.* 24 (2002) 1861–1884, doi:[10.1016/S0191-8141\(02\)00035-4](https://doi.org/10.1016/S0191-8141(02)00035-4).
- [15] P. Duval, Creep and recrystallization of polycrystalline ice, *Bull. Minéralogie*. 102 (1979) 80–85, doi:[10.3406/bulmi.1979.7258](https://doi.org/10.3406/bulmi.1979.7258).
- [16] J. Weertman, Creep Deformation of Ice, *Annu. Rev. Earth Planet. Sci.* 11 (1983) 215–240, doi:[10.1146/annurev.ea.11.050183.001243](https://doi.org/10.1146/annurev.ea.11.050183.001243).
- [17] B. Derby, M.F. Ashby, On dynamic recrystallisation, *Scr. Metall.* 21 (1987) 879–884, doi:[10.1016/0036-9748\(87\)90341-3](https://doi.org/10.1016/0036-9748(87)90341-3).
- [18] W.F. Budd, T.H. Jacka, A review of ice rheology for ice sheet modelling, *Cold Reg. Sci. Technol.* 16 (1989) 107–144, doi:[10.1016/0165-232X\(89\)90014-1](https://doi.org/10.1016/0165-232X(89)90014-1).
- [19] R.B. Alley, Flow-law hypotheses for ice-sheet modeling, *J. Glaciol.* 38 (1992) 245–256, doi:[10.3189/S0022143000003658](https://doi.org/10.3189/S0022143000003658).
- [20] W.F. Budd, R.C. Warner, T.H. Jacka, J. Li, A. Treverrow, Ice flow relations for stress and strain-rate components from combined shear and compression laboratory experiments, *J. Glaciol.* 59 (2013) 374–392, doi:[10.3189/2013jog12j106](https://doi.org/10.3189/2013jog12j106).
- [21] M. Mellor, D.M. Cole, Deformation and failure of ice under constant stress or constant strain-rate, *Cold Reg. Sci. Technol.* 5 (1982) 201–219, doi:[10.1016/0165-232X\(82\)90015-5](https://doi.org/10.1016/0165-232X(82)90015-5).
- [22] W.B. Durham, H.C. Heard, S.H. Kirby, Experimental deformation of polycrystalline H₂O ice at high pressure and low temperature: preliminary results, *J. Geophys. Res.* 88 (1983) B377, doi:[10.1029/JB088iS01p0B377](https://doi.org/10.1029/JB088iS01p0B377).
- [23] E.H. Rutter, K.H. Brodie, The role of tectonic grain size reduction in the rheological stratification of the lithosphere, *Geol. Rundschau*. 77 (1988) 295–307, doi:[10.1007/BF01848691](https://doi.org/10.1007/BF01848691).
- [24] E.J.N. Kuiper, I. Weikusat, J.H.P. De Bresser, D. Jansen, G.M. Pennock, M.R. Drury, Using a composite flow law to model deformation in the NEEM deep ice core, Greenland-Part 1: the role of grain size and grain size distribution on deformation of the upper 2207&thinspm, *Cryosphere* 14 (2020) 2429–2448, doi:[10.5194/tc-14-2429-2020](https://doi.org/10.5194/tc-14-2429-2020).
- [25] L.R. Campbell, L. Menegon, Transient High Strain Rate During Localized Viscous Creep in the Dry Lower Continental Crust (Lofoten, Norway), *J. Geophys. Res. Solid Earth*. 124 (2019) 10240–10260, doi:[10.1029/2019JB018052](https://doi.org/10.1029/2019JB018052).
- [26] P. Duval, C. Lorius, Crystal size and climatic record down to the last ice age from Antarctic ice, *Earth Planet. Sci. Lett.* 48 (1980) 59–64, doi:[10.1016/0012-821X\(80\)90170-3](https://doi.org/10.1016/0012-821X(80)90170-3).
- [27] S. De La Chapelle, O. Castelnaud, V. Lipenkov, P. Duval, Dynamic recrystallization and texture development in ice as revealed by the study of deep ice cores in Antarctica and Greenland, *J. Geophys. Res. Solid Earth*. 103 (1998) 5091–5105, doi:[10.1029/97jb02621](https://doi.org/10.1029/97jb02621).
- [28] M. Montagnat, O. Castelnaud, P.D. Bons, S.H. Faria, O. Gagliardini, F. Gillet-Chaulet, F. Grennerat, A. Gria, R.A. Lebensohn, H. Moulinec, J. Roessiger, P. Suquet, Multiscale modeling of ice deformation behavior, *J. Struct. Geol.* 61 (2014) 78–108, doi:[10.1016/j.jsg.2013.05.002](https://doi.org/10.1016/j.jsg.2013.05.002).
- [29] D. Iliescu, I. Baker, H. Chang, Determining the orientations of ice crystals using electron backscatter patterns, *Microsc. Res. Tech.* 63 (2004) 183–187, doi:[10.1002/jemt.20029](https://doi.org/10.1002/jemt.20029).
- [30] R. Obbard, I. Baker, K. Sieg, Using electron backscatter diffraction patterns to examine recrystallization in polar ice sheets, *J. Glaciol.* 52 (2006) 546–557, doi:[10.3189/172756506781828458](https://doi.org/10.3189/172756506781828458).
- [31] C.L. Hulbe, T.A. Scambos, M. Klingler, M.A. Fahnestock, Flow variability and ongoing margin shifts on Bindschadler and MacAyeal Ice Streams, West Antarctica, *J. Geophys. Res. Earth Surf.* 121 (2016) 283–293, doi:[10.1002/2015JF003670](https://doi.org/10.1002/2015JF003670).
- [32] M. Stipp, The recrystallized grain size piezometer for quartz, *Geophys. Res. Lett.* 30 (2003) 2088, doi:[10.1029/2003GL018444](https://doi.org/10.1029/2003GL018444).
- [33] M. Stipp, J. Tullis, M. Scherwath, J.H. Behrmann, A new perspective on paleopiezometry: dynamically recrystallized grain size distributions indicate mechanism changes, *Geology* 38 (2010) 759–762, doi:[10.1130/G31162.1](https://doi.org/10.1130/G31162.1).
- [34] G.P. Rigsby, The Complexities of the Three-Dimensional Shape of Individual Crystals in Glacier Ice, *J. Glaciol.* 7 (1968) 233–251, doi:[10.3189/S0022143000031026](https://doi.org/10.3189/S0022143000031026).
- [35] R.L. Hooke, P.J. Hudleston, Ice Fabrics in a Vertical Flow Plane, Barnes Ice Cap, Canada, *J. Glaciol.* 25 (1980) 195–214, doi:[10.3189/s0022143000010443](https://doi.org/10.3189/s0022143000010443).
- [36] M.E. Monz, P.J. Hudleston, D.J. Prior, Z. Michels, S. Fan, M. Negrini, P.J. Langhorne, C. Qi, in: *Full Crystallographic Orientation (c and a axes) of warm, Coarse-Grained Ice in a Shear-Dominated setting: a Case Study*, 15, Cryosph, Storgläciären, Sweden, 2021, pp. 303–324, doi:[10.5194/tc-15-303-2021](https://doi.org/10.5194/tc-15-303-2021).
- [37] S. Karato, M. Toriumi, T. Fujii, Dynamic recrystallization of olivine single crystals during high-temperature creep, *Geophys. Res. Lett.* 7 (1980) 649–652, doi:[10.1029/GL007i009p00649](https://doi.org/10.1029/GL007i009p00649).
- [38] D.L. Kohlstedt, M.S. Weathers, Deformation-induced microstructures, paleopiezometers, and differential stresses in deeply eroded fault zones, *J. Geophys. Res.* 85 (1980) 6269–6285, doi:[10.1029/JB085iB11p06269](https://doi.org/10.1029/JB085iB11p06269).
- [39] A.J. Cross, D.J. Prior, M. Stipp, S. Kidder, The recrystallized grain size piezometer for quartz: an EBSD-based calibration, *Geophys. Res. Lett.* 44 (2017) 6667–6674, doi:[10.1002/2017GL073836](https://doi.org/10.1002/2017GL073836).
- [40] M. Stipp, J. Tullis, H. Behrens, Effect of water on the dislocation creep microstructure and flow stress of quartz and implications for the recrystallized grain size piezometer, *J. Geophys. Res.* 111 (2006) B04201, doi:[10.1029/2005JB003852](https://doi.org/10.1029/2005JB003852).
- [41] R.J. Twiss, Theory and Applicability of a Recrystallized Grain Size Paleopiezometer, in: *Stress Earth*, Birkhäuser Basel, Basel, 1977, pp. 227–244, doi:[10.1007/978-3-0348-5745-1_13](https://doi.org/10.1007/978-3-0348-5745-1_13).
- [42] J.-C.C. Mercier, D.A. Anderson, N.L. Carter, Stress in the lithosphere: inferences from steady state flow of rocks, *Pure Appl. Geophys. Pageoph* 115 (1977) 199–226, doi:[10.1007/BF01637104](https://doi.org/10.1007/BF01637104).
- [43] C. Goetze, D.L. Kohlstedt, Laboratory study of dislocation climb and diffusion in olivine, *J. Geophys. Res.* 78 (1973) 5961–5971, doi:[10.1029/JB078i026p05961](https://doi.org/10.1029/JB078i026p05961).
- [44] D.P. Field, Quantification of partially recrystallized polycrystals using electron backscatter diffraction, *Mater. Sci. Eng. A*. 190 (1995) 241–246, doi:[10.1016/0921-5093\(94\)09601-R](https://doi.org/10.1016/0921-5093(94)09601-R).
- [45] R. Heilbronner, S. Barrett, *Image Analysis in Earth Sciences*, Springer Berlin Heidelberg, Berlin, Heidelberg, 2014, doi:[10.1007/978-3-642-10343-8](https://doi.org/10.1007/978-3-642-10343-8).
- [46] J. Tullis, R.A. Yund, Dynamic recrystallization of feldspar: a mechanism for ductile shear zone formation, *Geology* 13 (1985) 238, doi:[10.1130/0091-7613\(1985\)13\(238:DROFAM\)2.0.CO;2](https://doi.org/10.1130/0091-7613(1985)13(238:DROFAM)2.0.CO;2).
- [47] M.J. Vaughan, D.J. Prior, M. Jefferd, N. Brantut, T.M. Mitchell, M. Seidemann, Insights into anisotropy development and weakening of ice from in situ P wave velocity monitoring during laboratory creep, *J. Geophys. Res. Solid Earth*. 122 (2017) 7076–7089, doi:[10.1002/2017JB013964](https://doi.org/10.1002/2017JB013964).
- [48] A.J. Cross, P. Skemer, Rates of Dynamic Recrystallization in Geologic Materials, *J. Geophys. Res. Solid Earth*. 124 (2019) 1324–1342, doi:[10.1029/2018JB016201](https://doi.org/10.1029/2018JB016201).
- [49] J.H. Kruhl, M. Nega, The fractal shape of sutured quartz grain boundaries: application as a geothermometer, *Int. J. Earth Sci.* 85 (1996) 38–43, doi:[10.1007/bf00192058](https://doi.org/10.1007/bf00192058).
- [50] M. Takahashi, H. Nagahama, T. Masuda, A. Fujimura, Fractal analysis of experimentally, dynamically recrystallized quartz grains and its possible application as a strain rate meter, *J. Struct. Geol.* 20 (1998) 269–275, doi:[10.1016/S0191-8141\(97\)00072-2](https://doi.org/10.1016/S0191-8141(97)00072-2).
- [51] R. Heilbronner, S. Barrett, *Image Analysis in Earth Sciences*, Springer, 2014.
- [52] I. Hamann, C. Weikusat, N. Azuma, S. Kipfstuhl, Evolution of ice crystal microstructure during creep experiments, *J. Glaciol.* 53 (2007) 479–489, doi:[10.3189/002214307783258341](https://doi.org/10.3189/002214307783258341).
- [53] P. Duval, O. Castelnaud, Dynamic Recrystallization of Ice in Polar Ice Sheets, *Le J. Phys. IV*. 05 (1995) C3-197–C3-205, doi:[10.1051/jp4:1995317](https://doi.org/10.1051/jp4:1995317).
- [54] D.M. Cole, Preparation of polycrystalline ice specimens for laboratory experiments, *Cold Reg. Sci. Technol.* 1 (1979) 153–159, doi:[10.1016/0165-232X\(79\)90007-7](https://doi.org/10.1016/0165-232X(79)90007-7).
- [55] L.A. Stern, W.B. Durham, S.H. Kirby, Grain-size-induced weakening of H₂O ices I and II and associated anisotropic recrystallization, *J. Geophys. Res. Solid Earth*. 102 (1997) 5313–5325, doi:[10.1029/96JB03894](https://doi.org/10.1029/96JB03894).
- [56] T.H. Jacka, J. Li, Flow rates and crystal orientation fabrics in compression of polycrystalline ice at low temperatures and stresses, in: *Int. Symp. Phys. Ice Core Rec*, Hokkaido University Press, 2000, pp. 83–102. <http://hdl.handle.net/2115/32463>.
- [57] C. Qi, D.J. Prior, L. Craw, S. Fan, M.-G. Llorens, A. Gria, M. Negrini, P.D. Bons, D.L. Goldsby, Crystallographic preferred orientations of ice deformed in direct-shear experiments at low temperatures, *Cryosph* 13 (2019) 351–371, doi:[10.5194/tc-13-351-2019](https://doi.org/10.5194/tc-13-351-2019).

- [58] H.C. Heard, W.B. Durham, C.O. Boro, S.H. Kirby, A triaxial deformation apparatus for service at $77 \leq T \leq 273$ K, *Brittle-Ductile Transit. Rocks* (1990) 225–228, doi:[10.1029/GM056p0225](https://doi.org/10.1029/GM056p0225).
- [59] T. Chauve, M. Montagnat, F. Barou, K. Hidas, A. Tommasi, D. Mainprice, Investigation of nucleation processes during dynamic recrystallization of ice using cryo-EBSD, *Philos. Trans. R. Soc. A Math. Phys. Eng. Sci.* 375 (2017) 20150345, doi:[10.1098/rsta.2015.0345](https://doi.org/10.1098/rsta.2015.0345).
- [60] D.J. Prior, K. Lilly, M. Seidemann, M. Vaughan, L. Becroft, R. Easingwood, S. Diebold, R. Obbard, C. Daghlain, I. Baker, T. Caswell, N. Golding, D. Goldsby, W.B. Durham, S. Piazzolo, C.J.L. WILSON, Making EBSD on water ice routine, *J. Microsc.* 259 (2015) 237–256, doi:[10.1111/jmi.12258](https://doi.org/10.1111/jmi.12258).
- [61] F. Bachmann, R. Hielscher, H. Schaeben, Grain detection from 2d and 3d EBSD data—Specification of the MTEX algorithm, *Ultramicroscopy* 111 (2011) 1720–1733, doi:[10.1016/j.ultramic.2011.08.002](https://doi.org/10.1016/j.ultramic.2011.08.002).
- [62] D. Mainprice, F. Bachmann, R. Hielscher, H. Schaeben, Descriptive tools for the analysis of texture projects with large datasets using MTEX: strength, symmetry and components, *Geol. Soc. London, Spec. Publ.* 409 (2015) 251–271, doi:[10.1144/SP409.8](https://doi.org/10.1144/SP409.8).
- [63] A. Kolmogorov, *Statistical theory of crystallization of metals*, *Bull. Acad. Sci. USSR Ser. Math.* 1 (1937) 355–359.
- [64] M. Avrami, Kinetics of phase change. I: general theory, *J. Chem. Phys.* 7 (1939) 1103–1112, doi:[10.1063/1.1750380](https://doi.org/10.1063/1.1750380).
- [65] W.A. Johnson, R.F. Mehl, Reaction kinetics in processes of nucleation and growth, *Trans. Am. Inst. Min. Metall. Eng.* 135 (1939) 416–442.
- [66] R. Sandström, R. Lagneborg, A model for static recrystallization after hot deformation, *Acta Metall.* 23 (1975) 481–488, doi:[10.1016/0001-6160\(75\)90087-5](https://doi.org/10.1016/0001-6160(75)90087-5).
- [67] C.W. Price, Use of Kolmogorov-Johnson-Mehl-Avrami kinetics in recrystallization of metals and crystallization of metallic glasses, *Acta Metall. Mater.* 38 (1990) 727–738, doi:[10.1016/0956-7151\(90\)90024-B](https://doi.org/10.1016/0956-7151(90)90024-B).
- [68] A.I. Fernández, P. Uranga, B. López, J.M. Rodríguez-Ibabe, Dynamic recrystallization behavior covering a wide austenite grain size range in Nb and Nb-Ti microalloyed steels, *Mater. Sci. Eng. A.* 361 (2003) 367–376, doi:[10.1016/S0921-5093\(03\)00562-8](https://doi.org/10.1016/S0921-5093(03)00562-8).
- [69] J.J. Jonas, X. Quelennec, L. Jiang, É. Martin, The Avrami kinetics of dynamic recrystallization, *Acta Mater.* 57 (2009) 2748–2756, doi:[10.1016/j.actamat.2009.02.033](https://doi.org/10.1016/j.actamat.2009.02.033).
- [70] S. Steinemann, *Experimentelle Untersuchungen zur Plastizität von Eis*, ETH Zürich, 1958.
- [71] A.J. Gow, D.A. Meese, R.B. Alley, J.J. Fitzpatrick, S. Anandakrishnan, G.A. Woods, B.C. Elder, Physical and structural properties of the Greenland Ice Sheet Project 2 ice core: a review, *J. Geophys. Res. Ocean.* 102 (1997) 26559–26575, doi:[10.1029/97JC00165](https://doi.org/10.1029/97JC00165).
- [72] P. Duval, M. Montagnat, F. Grennerat, J. Weiss, J. Meyssonier, A. Philip, Creep and plasticity of glacier ice: a material science perspective, *J. Glaciol.* 56 (2011) 1059–1068, doi:[10.3189/002214311796406185](https://doi.org/10.3189/002214311796406185).
- [73] M. Montagnat, N. Azuma, D. Dahl-Jensen, J. Eichler, S. Fujita, F. Gillet-Chaulet, S. Kipfstuhl, D. Samyn, A. Svensson, I. Weikusat, Fabric along the NEEM ice core, Greenland, and its comparison with GRIP and NGRIP ice cores, *Cryosph. Res.* (2014) 1129–1138.
- [74] B. Derby, The dependence of grain size on stress during dynamic recrystallisation, *Acta Metall. Mater.* 39 (1991) 955–962, doi:[10.1016/0956-7151\(91\)90295-C](https://doi.org/10.1016/0956-7151(91)90295-C).
- [75] N.J. Austin, B. Evans, Paleowattmeters: a scaling relation for dynamically recrystallized grain size, *Geology* 35 (2007) 343–344, doi:[10.1130/G23244A](https://doi.org/10.1130/G23244A).
- [76] I. Shimizu, Theories and applicability of grain size piezometers: the role of dynamic recrystallization mechanisms, *J. Struct. Geol.* 30 (2008) 899–917, doi:[10.1016/j.jsg.2008.03.004](https://doi.org/10.1016/j.jsg.2008.03.004).
- [77] D.L. Sahagian, A.A. Proussevitch, 3D particle size distributions from 2D observations: stereology for natural applications, *J. Volcanol. Geotherm. Res.* 84 (1998) 173–196, doi:[10.1016/S0377-0273\(98\)00043-2](https://doi.org/10.1016/S0377-0273(98)00043-2).
- [78] R. Heilbronner, D. Bruhn, The influence of three-dimensional grain size distributions on the rheology of polyphase rocks, *J. Struct. Geol.* 20 (1998) 695–705, doi:[10.1016/S0191-8141\(98\)00010-8](https://doi.org/10.1016/S0191-8141(98)00010-8).
- [79] M.A. Lopez-Sanchez, Which average, how many grains, and how to estimate robust confidence intervals in unimodal grain size populations, *J. Struct. Geol.* 135 (2020) 104042, doi:[10.1016/j.jsg.2020.104042](https://doi.org/10.1016/j.jsg.2020.104042).
- [80] R.C. Gifkins, Grain-boundary sliding and its accommodation during creep and superplasticity, *Metall. Trans. A.* 7 (1976) 1225–1232, doi:[10.1007/BF02656607](https://doi.org/10.1007/BF02656607).
- [81] E.I. Poliak, J.J. Jonas, A one-parameter approach to determining the critical conditions for the initiation of dynamic recrystallization, *Acta Mater.* 44 (1996) 127–136, doi:[10.1016/1359-6454\(95\)00146-7](https://doi.org/10.1016/1359-6454(95)00146-7).
- [82] N. Azuma, T. Miyakoshi, S. Yokoyama, M. Takata, Impeding effect of air bubbles on normal grain growth of ice, *J. Struct. Geol.* 42 (2012) 184–193, doi:[10.1016/j.jsg.2012.05.005](https://doi.org/10.1016/j.jsg.2012.05.005).
- [83] S. Karato, *Deformation of Earth Materials: An Introduction to the Rheology of Solid Earth*, Cambridge University Press, 2008.
- [84] J.E. Bailey, P.B. Hirsch, The dislocation distribution, flow stress, and stored energy in cold-worked polycrystalline silver, *Philos. Mag.* 5 (1960) 485–497, doi:[10.1080/14786436008238300](https://doi.org/10.1080/14786436008238300).
- [85] O. Ajaja, Role of recovery in high temperature constant strain rate deformation, *J. Mater. Sci.* 26 (1991) 6599–6605, doi:[10.1007/BF02402651](https://doi.org/10.1007/BF02402651).
- [86] P. Duval, M.F. Ashby, I. Anderman, Rate-controlling processes in the creep of polycrystalline ice, *J. Phys. Chem.* 87 (1983) 4066–4074, doi:[10.1021/j100244a014](https://doi.org/10.1021/j100244a014).
- [87] O.B. Nasello, C.L. Di Prinzio, P.G. Guzmán, Temperature dependence of “pure” ice grain boundary mobility, *Acta Mater.* 53 (2005) 4863–4869, doi:[10.1016/j.actamat.2005.06.022](https://doi.org/10.1016/j.actamat.2005.06.022).
- [88] J.E. Burke, D. Turnbull, Recrystallization and grain growth, *Prog. Met. Phys.* 3 (1952) 220–244.
- [89] W.S.B. Paterson, *The Physics of Glaciers*, Third, Elsevier, 1994.
- [90] H.-J. Kim, C.V. Thompson, The effects of dopants on surface-energy-driven secondary grain growth in silicon films, *J. Appl. Phys.* 67 (1990) 757–767, doi:[10.1063/1.345756](https://doi.org/10.1063/1.345756).
- [91] H.P. Longworth, C.V. Thompson, Abnormal grain growth in aluminum alloy thin films, *J. Appl. Phys.* 69 (1991) 3929–3940, doi:[10.1063/1.348452](https://doi.org/10.1063/1.348452).
- [92] J.-M. Zhang, K.-W. Xu, V. Ji, Competition between surface and strain energy during grain growth in free-standing and attached Ag and Cu films on Si substrates, *Appl. Surf. Sci.* 187 (2002) 60–67, doi:[10.1016/S0169-4332\(01\)00782-6](https://doi.org/10.1016/S0169-4332(01)00782-6).